

Developing FTIR Microspectroscopy for the Analysis of Animal-Tissue Residues on Stone Tools

Gilliane Monnier¹  · Ellery Frahm^{1,2} · Bing Luo³ · Kele Missal¹

Published online: 9 March 2017

© Springer Science+Business Media New York 2017

Abstract The analysis of microscopic residues on stone tools provides one of the most direct ways to reconstruct the functions of such artifacts. However, new methods are needed to strengthen residue identifications based upon visible-light microscopy. In this work, we establish that reflectance Fourier-transform infrared microspectroscopy (FTIRM) can be used to document IR spectra of animal-tissue residues on experimental stone tools. First, we present a set of reflectance FTIRM standards for the most commonly identified animal-tissue residues on stone tools: skin, meat, fat, hair, blood, feather barbules, fish scales, and bone. We provide spectral peak assignments for each residue and demonstrate that high-quality reflectance FTIRM spectra can be generated under ideal circumstances. Second, we document the spectra for these residues when they are located on a stone substrate such as flint or obsidian. We discuss procedures for correcting spectra that are affected by specular reflection and explain the effects of spectral interference from the stone. Our results show that reflectance FTIRM is sensitive to small intra-sample differences in composition. This means that it will record the effects of decomposition in ancient residues. The methodological developments we present here will help lithic residue analysts incorporate in situ reflectance FTIRM into their analysis protocols to strengthen identifications.

Electronic supplementary material The online version of this article (doi:10.1007/s10816-017-9325-3) contains supplementary material, which is available to authorized users.

✉ Gilliane Monnier
monni003@umn.edu

¹ Department of Anthropology, University of Minnesota, 395 Hubert Humphrey Center, 301 19th Ave. South, Minneapolis, MN 55455, USA

² Yale Initiative for the Study of Ancient Pyrotechnology, Department of Anthropology, Yale University, P.O. Box 208277, New Haven, CT 06520, USA

³ Characterization Facility, University of Minnesota, 12 Shepherd Labs, 100 Union St. SE, Minneapolis, MN 55455, USA

Keywords FTIR microspectroscopy · residue analysis · lithic analysis

Introduction

One of the most direct sources of information about stone tool use during the Paleolithic comes from lithic residue analysis, which aims to identify microscopic fragments of plant and animal tissue adhered to the tools' surfaces. Such residues are assumed to originate from materials that, when worked using the tool, became caught on sharp edges and in flake scars. Under conditions of favorable preservation, these residues, as well as hafting adhesives such as resins, gums, and pitches, are thought to have been preserved for tens of thousands of years. Residues have been observed in situ (on stone tools) using high-powered microscopy, potentially providing valuable information about the behavior and activities of the humans who used them (*e.g.*, Lombard 2011, Hardy *et al.* 2013). Despite its inherent appeal, however, lithic residue analysis faces the following challenges:

1. Identification

How can the human eye (aided by light microscopes) accurately identify often featureless, amorphous, severely degraded microscopic fragments of plant and animal tissue? It is true that some biological tissues, such as hair, possess distinctive structural features that enable their identification with a high degree of certainty using visible-light microscopy (VLM) (*e.g.*, Croft *et al.* 2016). Most residues, however, lack such features, and their identification is subjective. We have previously shown that ambiguity in identification exists even for fresh experimental residues (Monnier *et al.* 2012); in our tests, identifications of fresh residues based on VLM alone were, on average, incorrect ~25% of the time.

2. Preservation

How can organic residues be preserved for tens of thousands of years in the absence of exceptional circumstances (*i.e.*, anhydrous or anoxic environments)? As noted by Weiner (2010:207), uncharred organic matter is rapidly degraded by microorganisms in most environments. Biological molecules are preserved only if they are protected from microbial activity and chemical degradation; in other words, if they are located in a “protected niche” within the mineral phase of materials such as bone, teeth, eggshells, and phytoliths (*ibid.*). Controlled experiments by Langejans (2010) and Croft *et al.* (2016) designed to investigate the preservation of residues on stone tools support these observations by showing that animal and plant tissues decay rapidly in most circumstances. Langejans (2010) showed that, while the rate of decay of residues on stone tools placed in sheltered environments is lower than that of residues placed in open-air contexts, close to half of the residues in these environments have decayed after only 1 year. Applying the same preservation index, Croft *et al.* (2016) showed that organic residues on stone tools buried for 11 months in three different soils had decayed dramatically. Only keratinized tissues (hair and feathers) were preserved better than most.

These results raise the question of what mechanism is responsible for preserving residues for tens of thousands of years in environments that do not fulfill the criteria (*e.g.*, anoxic or anhydrous) normally associated with organic preservation.

3. Contamination

Contamination is a serious problem in the analysis of many types of archeological microremains, from charcoal and pollen to starch grains (*e.g.*, Crowther *et al.* 2014). It applies to lithic residue analysis as well. How do we know that observed residues are the product of tool-use behaviors rather than contamination? Recent research has documented common types of laboratory contaminants, such as skin flakes, starch grains, and modeling clay, which may be mistaken for residues (Pedergnana *et al.* 2016). Analysis of the residue patterning on buried experimental tools yielded a contextual approach to interpreting residues based upon their association with working edges (Langejans 2011). These studies provide valuable contributions to residue analysts seeking to mitigate the effects of contamination.

Continued research in each of these three areas is fundamentally important for progress to continue to be made in lithic residue analysis. Our focus in this paper is on the first one, identification, which is foundational. In earlier research, we demonstrated that lithic residue analysis based upon visible-light microscopy (VLM) alone is insufficient, and we began to develop complementary methods using electron and vibrational microscopy (Monnier *et al.* 2012, 2013). We identified Fourier-transform infrared microspectroscopy (FTIRM) as a technique with great potential to provide chemical information about residues in a non-destructive manner. This analytical technique generates infrared (IR) spectra of substances, in either transmission or reflectance mode, that are placed on the stage of a specialized microscope attached to an FTIR bench. The resulting spectra contain detailed information about the chemical structure of the specimen. Its advantage, *vis-à-vis* the more well-known analytical technique of FTIR spectroscopy, is that it is non-destructive, requires no sample preparation, and can be used to characterize extremely small (<200 μm in diameter with a $\times 15$ objective) residues. It is particularly suitable for lithic residue analysis because IR spectra can be collected from residues without removing them from the artifact. This is preferable to techniques in which residues are removed and destroyed for two main reasons: (1) the context of the residues (*i.e.*, their locations on the tool) is preserved and (2) the residues can also be studied using other methods. *In situ* FTIRM analysis, however, has proved to be challenging (Cesaro and Lemorini 2012; Monnier *et al.* 2013; Prinsloo *et al.* 2014). First, reflectance FTIRM spectra cannot be assumed to be equivalent to IR spectra obtained using other methods, such as transmission FTIR spectroscopy on specimens prepared as potassium bromide (KBr) pellets, or attenuated total reflectance (ATR)-FTIR. Second, reflectance FTIRM spectra of residues on stone tools are often affected by the stone that both underlies and surrounds the residue. This factor can result in the appearance of atypical spectral bands and greatly increased signal noise.

To address these challenges and to provide the next step in FTIRM method development, we carried out a project designed to:

- 1) Create a reference library of reflectance spectra of common Paleolithic stone tool residue types
- 2) Document the variability of these spectra on various stone substrates.

The purpose of the first goal was to yield a collection of IR standards (for ourselves and for others), based on known residues, against which archeological spectra can be compared. An important objective of this portion of the research was to test the viability of reflectance FTIRM. The purpose of the second goal was to better understand the effects of stone substrates on reflectance FTIRM spectra of residues.

Earlier, we published the results of our work developing a reference library of reflectance spectra of plant tissues (Monnier *et al.* 2017). These reference spectra are available online at <http://z.umn.edu/ftir>. In this paper, we focus on animal-tissue residues which have been documented in Paleolithic contexts but are difficult to positively identify using VLM alone. We discuss the structure and chemical composition of each animal tissue type and identify the major peaks in their IR spectra; we provide a reference library of reflectance FTIRM spectra for meat, fat, skin, blood, hair, feather barbules and calamus, bone, and fish scales (also online in our database). We also document and explain the reflectance FTIRM spectra collected from these animal tissues when they are located on a siliceous stone substrate.

Our overall goal is increased accuracy and reproducibility of residue identification so that we can more confidently reconstruct past tool-using behaviors while, at the same time, address the issues of residue preservation, degradation, and contamination. We see the development of objective, quantifiable, and repeatable means of residue identification as an essential step towards the development of a scientific methodology of residue analysis.

Materials and Methods

Materials

For several decades, lithic residue analysts working on Paleolithic and later assemblages have identified, using VLM and other methods, the following animal-based residues on stone tools: blood (Loy and Dixon 1998; Loy and Hardy 1992; Robertson *et al.* 2009; Williamson 2004; Lombard 2005, 2008, 2011, 2014), bone (Hardy *et al.* 2008, Hardy *et al.* 2013, Hardy and Moncel 2011; Lombard 2008), fat (Lombard 2005, 2008, 2011), collagen (Lombard 2005, 2008, 2011; Hardy *et al.* 2013; Stephenson 2015), muscle or “animal tissue” (*ibid.*; Hardy and Moncel 2011), feathers (Hardy *et al.* 2001, 2008, Hardy *et al.* 2013; Hardy 2004, Hardy and Moncel 2011), fish scales (Hardy and Moncel 2011, Hardy *et al.* 2013), and mammalian hair (Hardy 2004; Hardy *et al.* 2001, 2008, Hardy *et al.* 2013; Hardy and Moncel 2011; Lombard 2008; Sobolik 1996). For our experiments, we mimicked these categories of residues, producing specimens of hair, skin, fat, blood, meat, bone, feathers, and fish scales (Fig. 1). We used these animal tissues to produce reflectance and transmission FTIRM standards and, subsequently, for our investigation of FTIRM spectra of residues on stone flakes.

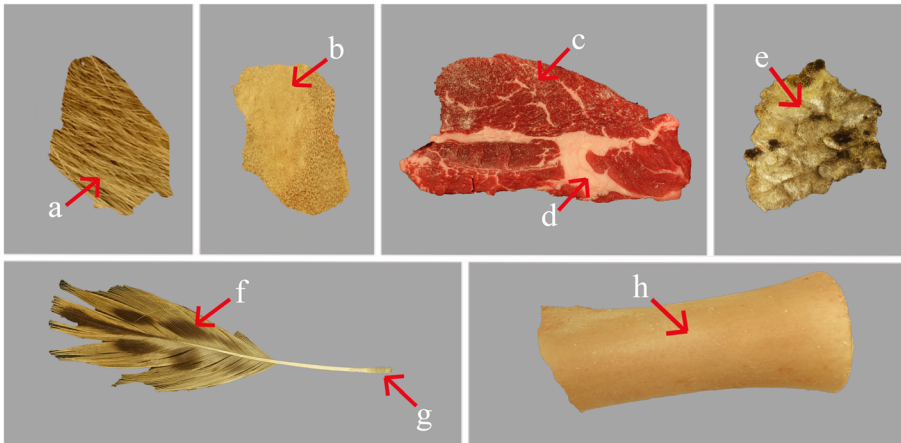


Fig. 1 Materials used to make experimental residues in this study: **a** deer hair, **b** deer skin (photograph is of a tanned deer hide, but we used an untanned hide in our experiments), **c** beef meat, **d** beef fat, **e** trout fish scales, **f** duck feather barbules, **g** duck feather calamus, and **h** beef bone

Skin

To obtain a sample of skin such as would occur on a stone tool used to scrape a hide, we used the untanned skin of a deer (*Odocoileus virginianus*) that was frozen and thawed. We scraped away the visible subcutaneous fat from the inside of the skin and sampled the dermal layer to prepare as a residue (procedure described below).

In order to understand the absorbance peaks in the resulting IR spectrum, it is useful to describe the structure and composition of skin. Mammalian skin is an extremely complex organ, and our treatment of it here will be greatly simplified. In general, skin consists of the epidermis and dermis. The epidermis, which is the outermost layer of the integument, protects the organism from the environment. It consists of a soft inner portion, called the Malpighian layer, and a hardened, cornified outer portion (Matoltsy 1986a). Epidermal cells form layers over the dermis. The dermis extends from the basal lamina of the epidermis to the penniculus adiposus, a layer of subcutaneous fat (Matoltsy 1986b). The dermis consists of a meshwork of fibrils embedded in a gel-like matrix called ground substance. It is traversed by blood vessels, nerves, hair follicles, lymphatic vessels, and several different types of glands. The dermal fibrils consist of three types: anchoring, elastic, and collagen fibrils. The gel matrix consists of proteoglycans, thread-like macromolecules with highly extended polysaccharide side chains. The gel has pores filled with water, protein, carbohydrate, and ions derived from blood (Matoltsy 1986b).

Collagen fibrils comprise ~70–80% of the dry weight of the dermis (Uitto 1986). Collagens are a family of closely related, genetically distinct proteins, rich in the amino acids hydroxyproline and hydroxylysine. They can be divided into several categories, all of which are characterized by a triple-helical conformation: collagen types I–III form broad-banded extracellular fibers called interstitial collagens. Collagen types IV–IX are minor collagens that do not form broad-banded fibers and are less abundant, although type IV collagen is a major component of the basement membranes in the skin and other tissues. Type I collagen fibers,

which are the most common fibril in the dermis, are composed of collagen molecules aligned in a quarter-stagger arrangement. Each collagen molecule is a rod-like structure, ~300 nm long, consisting of three polypeptide α -chains wrapped around each other in a triple helix (ibid.).

We expect skin residues on stone tools to consist of a complex and variable mixture of proteins (especially collagen), lipids, water, and proteoglycans.

Meat

One of the common categories of Paleolithic stone tool residues is expected to consist of fragments of meat, acquired from hunting and butchery activities. “Meat” is a catch-all phrase referring to the mass of muscle and connective tissue located between the skin and bones of mammalian prey. Although Paleolithic hominins clearly hunted and consumed meat from a wide variety of taxa, we chose beef steak to simulate meat residues. When sampling from the steak, we cut off a small piece from the muscle, avoiding visible fat and connective tissue.

We expect our “meat” residues to be primarily composed of skeletal muscle tissue. The anatomy of skeletal muscle tissue is well-documented: skeletal muscle is composed of bundles of fibers known as fascicles. The individual muscle fibers, known as myofibers, are cells which vary in diameter from 10 to 100 μm and in length from a few millimeters to several centimeters (Lieber 2002). The fibers and fascicles are surrounded by mesh-like sheaths of collagenous tissue. The myofiber cells contain a nucleus, mitochondria, and other cellular structures. In addition, their cytoplasm, known as the sarcoplasm, is rich in soluble proteins such as myoglobin; and also contains glycogen, lipids, and calcium ions. But the defining characteristic of muscle cells are myofibrils, filamentous components which run the entire length of the myofiber. Myofibrils are composed of myofilaments arranged into repeating subunits called sarcomeres, which are the functional unit of contraction (ibid.). The end-to-end arrangement of sarcomeres produces a banding pattern when muscle fibers are seen under VLM (e.g., Croft *et al.* 2016), leading to the widely known name “striated muscle” for skeletal muscle. Myofilaments, in turn, are composed of two types: thicker filaments containing myosin and thinner filaments containing actin. These two types of filaments interdigitate, forming a hexagonal array which comprises the sarcomere. Myosin molecules are large and highly asymmetrical, with a globular “motor” domain which powers muscle contraction at one end and a long tail at the other (ibid.). They polymerize to form thick filaments, from which the globular heads project. Actin filaments, on the other hand, are composed of a long α -helical arrangement of actin monomers, which are roughly spherical in shape and small compared to myosin. Their helical arrangement creates a groove along the filament’s length, which is filled by the regulatory proteins troponin and tropomyosin.

Meat of the type that we sampled, therefore, is expected to contain proteins (myosin and actin from the muscle fibers; myoglobin from the cytoplasm; hemoglobin from the capillaries which supply muscle tissue; and collagen from the connective tissue), water, and small amount of lipids, polysaccharides (e.g., glycogen), and ions (e.g., calcium).

Fat

We sampled fat from the same beef steaks we used for meat. The fat we sampled can be classified as inter- or intramuscular fat (Warriss 2010). Fat is defined as a connective tissue, known as adipose tissue, composed of fat cells or adipocytes. Mature adipocytes are composed of 98–99% triglyceride (ibid.). Triglycerides are formed by the combination of glycerol with three fatty acid molecules, which can be saturated (with carbon chains characterized by single bonds) or unsaturated (in which double bonds exist between some of the carbon atoms).

Subcutaneous beef fat is composed of 4% water, 1.5% protein, and 94% fat. We expect “fat” residues on stone tools to consist of a range of fatty acids.

Blood

Our blood sample was frozen beef blood, thawed at the time of preparation. Blood can be defined as a circulating connective tissue composed of two major components: (1) plasma, which makes up 65–70% by volume of bovine blood and which contains albumins, globins, mineral salts, and other solutes, and (2) cells, which make up the remainder, such as erythrocytes (red blood cells), leukocytes (white blood cells), and platelets (Duarte *et al.* 1999; Hortolà 2016). The main plasma proteins include albumins, immunoglobulins, α - and β -globulins, and fibrinogen. The most common cells are the erythrocytes, which are largely composed of the protein hemoglobin. The hemoglobin molecule is composed of two pairs of identical α and β subunits, each of which is composed of a protein chain tightly associated with a non-protein heme group (Fronticelli *et al.* 1995). Each protein chain contains eight α -helix structures, all of which have the same tertiary folding characteristic of globins; the molecule assumes a different conformation depending upon whether oxygen is bound or not to the molecule (ibid). Heme groups consist of porphyrin rings with covalently bonded iron atom at their centers. Therefore, blood residue of the type we created in our experiments is expected to contain, besides water and lipids, a variety of proteins such as serum albumin, hemoglobin, and globulins, as well as mineral salts and glucose.

Feathers

We used commercially purchased duck feathers for our experiments. We sampled two different parts of the feather: (1) the “quill” portion of the feather, known as the calamus, which inserts the feather into the follicle, and (2) downy feather barbules from the proximal portion of the feather vanes (the pennulas). The reason we sampled these two different feather structures is because we wished to create FTIRM standards for both given that barbules have been identified on stone tools from several sites (Hardy *et al.* 2001, 2008, Hardy *et al.* 2013; Hardy 2004; Hardy and Moncel 2011), and quill residues are expected to occur due to recent evidence which suggests humans may have cut feathers from birds (Finlayson *et al.* 2012, Morin and Laroulandie 2012).

Feathers are composed of ~90% protein, mostly beta (β) keratins (Stettenheim 2000). β -keratins are structural proteins of the epidermis found solely in reptiles and birds (Greenwold and Sawyer 2011). These fibrous proteins are composed of a crystalline-like filament and matrix structure formed by each single β -keratin molecule

(Fraser and Parry 2008). The molecular structure of feather keratin is a pleated sheet of four chains each of eight amino acid residues in length, arranged in a twisted, helical fashion, forming short rods (Gregg and Rogers 1986). We expect feather barbules and other feather parts to consist mostly of β -keratin.

Mammalian Hair

Our hair sample came from a tanned deer hide. We selected guard hairs only, and we took care not to include the follicle in the prepared sample. Nevertheless, it is possible that the hair contains substances from the hide tanning process, the specifics of which are unknown to us.

When hair is preserved, it is one of the most diagnostic of animal residues. Most mammals have an outer coat of large, thick hairs called guard hairs, and an inner coat of shorter, finer hairs known as underhair. There are usually multiple types of guard hair but only one type of underhair. The structure of hair consists of three cellular components: the cuticle, the cortex, and the central core or medulla. The cuticle consists of layers of flattened cells that form an overlapping, scale-like pattern, which is often quite distinctive according to species. Cuticle cells consist of an exocuticle of high sulfur content and an endocuticle of low sulfur content (Chapman 1986). Underneath the cuticle, the cortex consists of macrofibrils which are composed of α -keratin embedded in a sulfur-rich protein matrix (Feughelman 1997). Different species have different types of cortical cells, which seem to be associated with degree of crimping of the hair. Finally, the medulla, in the center of the hair shaft, consists of vacuolated cells; the cellular structure appears to be highly heterogeneous among species (*ibid.*).

The main protein component of mammalian hair, quills, nails, claws, hooves, and horns as well as the outermost layer of the epidermis, the stratum corneum, consists of α -keratins (Powell and Rogers 1986). Mammalian hair, wool, and quills are composed of so-called “hard” α -keratin fiber that makes up the hair cortex described above. The α -keratin macrofibrils are composed of cylindrical units called microfibrils, which, at the molecular level, consist of a complex axial and radial assembly of 50 nm-long heterodimers (Kreplak *et al.* 2004). The molecular structure of the heterodimers consists of a central rod composed of a double-stranded α -helical coiled-coil interrupted by nonhelical segments, surrounded by head and tail domains of unknown structure (*ibid.*). Hair also typically contains the pigments eumelanin and pheomelanin, complex polymers. Therefore, we expect the composition of hairs identified on stone tools to consist of α -keratin and pigments.

Bone

We selected a cow tibia, obtained defleshed and frozen, for these experiments. We first removed remaining meat as well as the periosteum before scraping the cortical bone for our samples. The structure of bone is well documented (*e.g.*, Weiner 2010:102–109) and is composed, on average, of 60–70% mineral content, 20% organic matter, and water. The mineral component of bone consists of carbonate hydroxylapatite, which forms very small, plate-like crystals (*ibid.*). The organic component of bone is mostly (~90%) composed of the protein type I collagen, with the remainder consisting of other proteins, proteoglycans, and lipids. The collagen fibrils are arranged into sheets, in-

between which the plate-shaped crystals are stacked. Different packing arrangements exist for the fibril arrays, depending on the type of bone (mineralized tendons, fetal bone, lamellar bone, and dentin). The infrared spectra of bone are well studied (e.g., Weiner 2010, Stiner *et al.* 2001, Acerbo *et al.* 2012) and document the presence of carbonate hydroxylapatite and collagen.

Fish Scales

We used scales from a Rainbow trout (*Oncorhynchus mykiss*), a teleost fish from the family Salmonidae. These fish have cycloid scales, which have been identified on stone tools (Hardy and Moncel 2011, Hardy *et al.* 2013). The structure of teleost fish scales has been extensively studied; they consist of an internal fibrillary plate covered by an external osseous layer (Ikoma *et al.* 2003). The internal plate is composed of collagen fibers (mainly type I collagen) that are aligned and organized into perpendicularly overlapping lamellae, producing a plywood pattern which lends strength and flexibility to the scale (Zylberberg *et al.* 1988, Ikoma *et al.* 2003). The external layer, initially composed of randomly arranged collagen fibers embedded in a proteoglycan matrix, gradually becomes mineralized as matrix vesicles produce crystals of calcium-deficient hydroxyapatite in random orientation. The internal layer gradually becomes calcified as well. In sum, from a chemical point of view, we can expect most teleost fish scales to consist primarily of collagen and hydroxyapatite.

Methods

One of our main goals was to produce a set of reflectance FTIRM standards of common residue types, documenting them first on an ideal substrate and then on stone flakes. Our sample preparation techniques are commensurate with this goal. The residue types described above were prepared by crushing and macerating a small amount (~1 mg) of sample using a clean, glass mortar and pestle and a small amount (~1 mL) of distilled water to obtain a homogeneous slurry. This served two purposes: it homogenized the samples, and it reduced particle sizes. Our previous work using plant residues shows that FTIRM is extremely sensitive to small compositional differences (Monnier *et al.* 2017); therefore, homogenizing the animal tissues during sample preparation was crucial. Additionally, it is well-known that smaller particle sizes result in higher-quality IR spectra, and our objective was to generate high-quality spectra for our library. We first produced pairs of residue samples suitable for transmission and reflectance FTIRM. Drops of the homogenized slurry were placed on (1) a polished, IR-invisible NaCl plate (Edmund Optics, Barrington, NJ, USA) for transmission microscopy, and (2) a reflective, aluminum (Al)-coated glass slide (borosilicate glass coated with a 100-nm-thick layer of Al, from Deposition Research Laboratories Inc., St. Charles, MO, USA), also IR invisible, for reflectance microscopy. The plates and slides were allowed to dry in a desiccator for several days before FTIR measurement.

In the second half of this study, we prepared slurries of each residue type in the same manner as described above and pipetted them onto sterilized flakes made of English ballast flint (which we categorized as “dark” or “light” colored), Texas chert, obsidian, and dacite. Since these samples were prepared at a later time by a different individual, slight compositional differences between the residues on stone versus the residues on

the aluminum-coated slides (henceforth referred to as “mirrored slides”) sometimes exist, resulting from minor differences in which the animal tissues under question were sampled.

In addition to FTIR microscopy, we also imaged these residues using VLM. Residues on the mirrored slides were imaged using a Leica MZ16A stereomicroscope equipped with a $\times 1.0$ plan apochromatic objective, whereas residues on the NaCl plates were imaged using a transmitted-light Leica DM2500 petrographic microscope. These images are available in our online database.

FTIRM spectra were gathered on a Nicolet Continuum FTIR microscope paired with a Nicolet iS50 FTIR bench. We operated the microscope in reflectance or transmission mode using the MCT detector, a KBr beamsplitter, and a resolution of 4 cm^{-1} , obtaining spectra from 4000 to 650 cm^{-1} wavenumbers. When possible, we opened the aperture to its maximum size of $150 \times 150\ \mu\text{m}$, but we sometimes reduced the aperture to decrease the signal from the stone substrate. Depending on the sample type and aperture size, we varied the number of scans from 200 to 5000. We also typically collected a minimum of three to eight spectra per sample (slide, plate, or stone) in order to document variability in the results.

Results

Assessing the Viability of Reflectance FTIRM, and Documenting IR Absorbance Peaks for Animal Tissue-Based Residues

Prinsloo *et al.* (2014) showed that reflectance FTIRM spectra of animal residues such as meat, fat, and bone on experimental stone tools are severely distorted relative to ATR spectra of the same residue types. They attributed these distortions, such as derivative and reststrahlen bands, to (1) optical issues inherent in reflectance FTIRM, (2) interference from the stone substrate, and (3) the thickness and surface texture of the residues. Their observations served as the impetus for our study, which was designed, as one goal, to gather reflectance spectra of residues on a substrate with nearly 100% reflection in the mid-infrared range (*i.e.*, polished Al). We sought to understand the precise nature of optical interference in reflectance spectroscopy as opposed to the more traditional transmission spectroscopy. To assess the quality of these spectra, we gathered three or more spectra from each residue prepared on mirrored slides using the FTIR microscope in reflectance mode. Then, we gathered several spectra from the same residue type prepared on NaCl plates using the FTIR microscope in transmission mode. This enabled us to directly compare the transmission FTIRM spectra, which are generally not expected to exhibit derivative bands or other spectral artifacts, with the reflectance FTIRM spectra in order to assess the quality of the latter. Representative FTIRM reflectance and transmission spectra for each residue category are presented in Figs. 2, 3, 4, 5, 6, 7, 8, and 9.

In addition to assessing the quality of the reflectance FTIRM spectra, which we found to be equivalent to that of transmission FTIRM spectra, we researched and assigned vibrational modes to the major peaks for each residue type (see Tables 1,2,3,4,5,6,7, and 8) and compared them with standards from external libraries. This showed that (1) our reflectance FTIRM spectra are in excellent agreement with

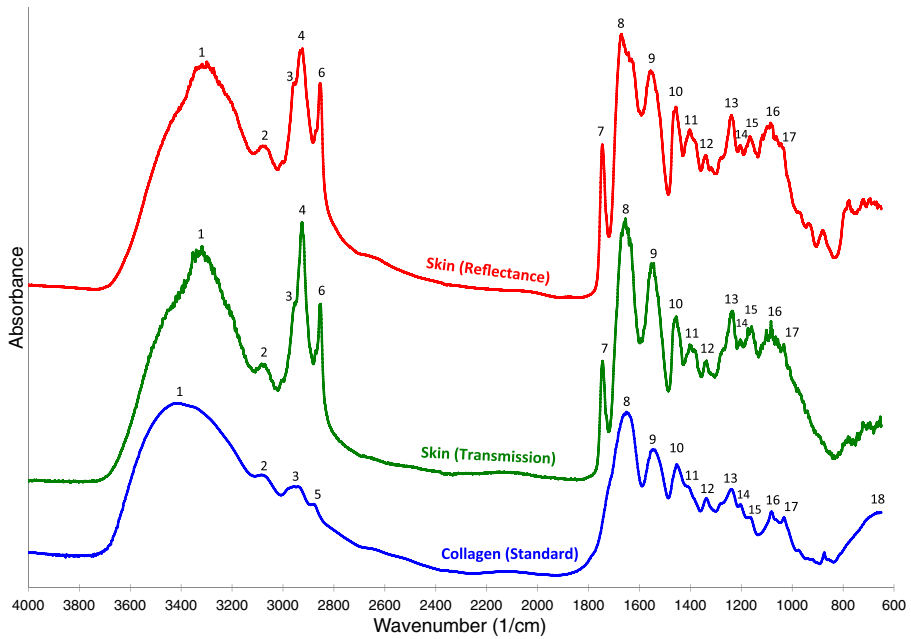


Fig. 2 FTIRM spectra of skin residue obtained in reflectance mode (on a mirrored slide) and in transmission mode (on a NaCl plate), compared with an FTIR standard for collagen (prepared using the KBr pellet method) from the Kimmel Center for Archaeological Science, Weizmann Institute of Science. Peak assignments are in Table 1. The reflectance spectrum (*red line*) is nearly identical to the transmission spectrum (*green line*); both clearly exhibit the protein peaks seen in the collagen standard (*blue line*). The reflectance spectrum is graphed in calculated absorbance mode ($\log(1/R)$). Note that spectra are plotted on the same scale, but have been vertically offset.

FTIR standards from independent libraries, and (2) that reflectance FTIRM spectra provide reliable chemical information. We now describe these results in detail for each category of animal residue.

Figure 2 shows the results for our “skin” residue category. The reflectance and transmission FTIRM spectra are virtually identical. Figure 2 also includes the spectrum for fresh collagen obtained from the on-line library of FTIR standards from the Kimmel Center for Archeological Science, Weizmann Institute of Science. This reference spectrum, like all other spectra from the Kimmel Center used in this study, was obtained on a sample prepared using the KBr pellet method. The vibrational modes we assigned to the absorption bands in these spectra are presented in Table 1. The correspondence between our skin spectra and the collagen spectrum is strong. The main differences between them are seen in (1) the presence of an extra peak at $\sim 1745\text{ cm}^{-1}$ (peak 7) in the skin spectra and (2) the relative intensities of the peaks located between 2960 and 2850 cm^{-1} (peaks 3–6). The greater relative absorbance in the skin spectra at peaks 3–6 reflects a greater contribution from CH_3 and CH_2 symmetric and asymmetric stretching in our skin sample than in pure collagen. This is probably due to the presence of lipids in the skin and is consistent with the strong peak at position #7, which represents stretching of the carbonyl functional group ($\text{C}=\text{O}$), found in fatty acids, among other compounds. There are a few other differences between the skin spectra and the collagen spectrum that likely reflect the fact skin contains substances other than collagen, as described earlier.

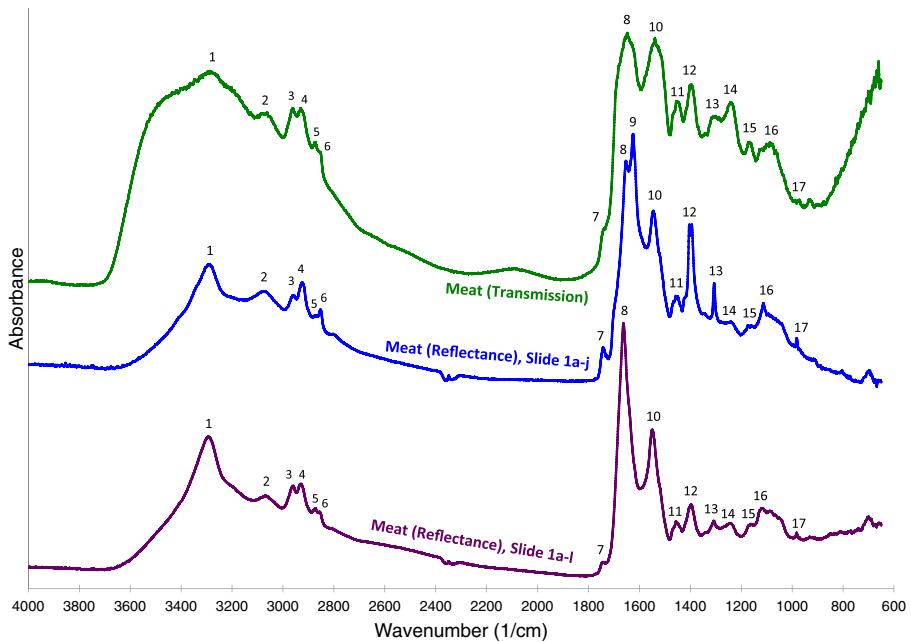


Fig. 3 FTIR spectra of meat residue obtained in reflectance mode (on mirrored slides) and in transmission mode (on a NaCl plate). Peak assignments are in Table 2. The two reflectance spectra illustrate small compositional differences between the two samples; the transmission spectrum is very similar to the other two, but contains more water (see text). The reflectance spectra are graphed in calculated absorbance mode ($\log(1/R)$). Note that spectra are plotted on the same scale, but have been vertically offset.

Figure 3 presents two reflectance FTIR spectra and one transmission FTIR spectrum that we obtained from beef meat. We specifically selected these spectra to demonstrate the kind of compositional variability that sometimes occurred in our samples, despite the steps taken to homogenize them. As described earlier, “meat” or skeletal muscle tissue is expected to contain a mix of different proteins (myosin, actin, myoglobin, hemoglobin, and collagen) and some lipids. This complex mix is responsible, we think, for the variability seen in Fig. 3, all of which stems from a single, ~ 2 -g piece of meat (peak locations and assignments are given in Table 2). The most prominent differences between the two reflectance spectra are at 1625 cm^{-1} (peak 9), where spectrum slide 1a–j exhibits a peak which is absent in slide 1a–l, and at 1395 cm^{-1} and 1306 cm^{-1} (peaks 12 and 13), where the peaks are much stronger and narrower on slide 1a–j than slide 1a–l. Spectrum slide 1a–j also has a slightly stronger peak at 1742 cm^{-1} (C = O stretching, peak 7), and at 2930 and 2850 cm^{-1} (CH_2 asymmetric and symmetric stretching; peaks 4 and 6). These relative intensity differences in the CH_x regions are perhaps due to different molecular orientations in the two samples. Both of these spectra exhibit similarities as well as differences with the transmission spectrum, which appears to contain more water, as evidenced by the strong shoulder at 3500 cm^{-1} (not labeled as a peak in the figure) attributable to OH stretching from water. The contribution from water is also seen at 1640 cm^{-1} where the OH bending absorption is significant and overlaps with the amide I peak (peak #8), contributing to its broadness. Although we did not have an FTIR spectrum for “meat” from an independent library to include in our figure, the spectra illustrated in Fig. 3 are entirely consistent with

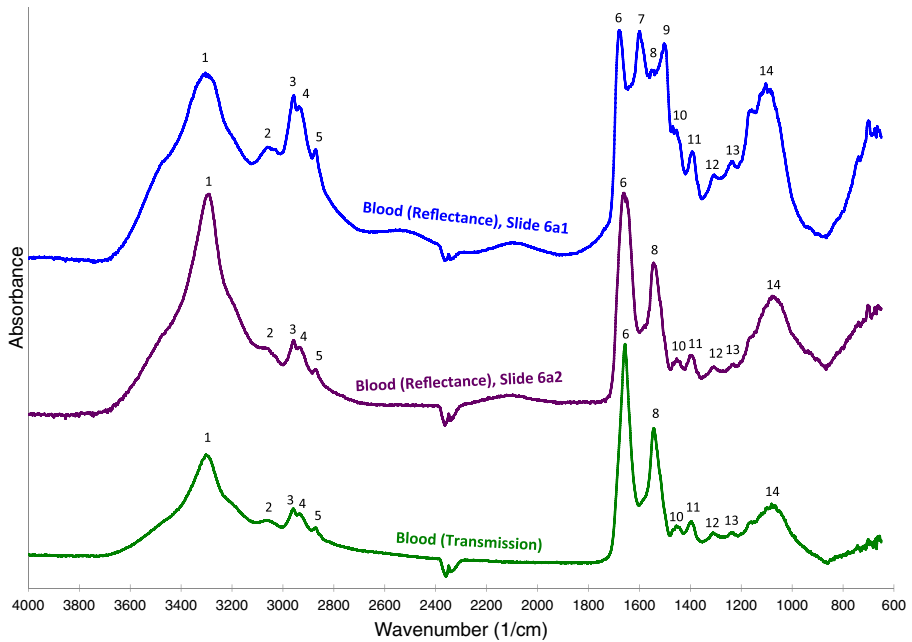


Fig. 4 FTIRM spectra of blood residue obtained in reflectance mode (on mirrored slides) and in transmission mode (on a NaCl plate). Peak assignments are in Table 3. The two reflectance spectra illustrate small compositional differences between the two samples; the transmission spectrum (*green line*) is nearly identical to reflectance spectrum Slide 6a3 (*purple line*). The reflectance spectra are graphed in calculated absorbance mode ($\log(1/R)$). Note that spectra are plotted on the same scale, but have been vertically offset.

published “meat” FTIR spectra (*e.g.*, Calabrò and Magazù 2014, Rahmania and Rohman 2015).

In Fig. 4, we present two reflectance FTIRM spectra obtained on beef blood as well as one transmission FTIRM spectrum (see Table 3 for peak assignments). There is very close agreement between the transmission spectrum and one of the reflectance spectra (slide 6a2). The other reflectance spectrum, slide 6a1, differs by the presence of two extra peaks at 1599 and 1503 cm^{-1} (peaks 7 and 9), as well as much stronger absorbance in the $2950\text{--}2850\text{ cm}^{-1}$ region. The 1599 and 1503 cm^{-1} peaks can be assigned to asymmetric $\text{C}(\text{O})\text{O}^-$ vibration and NH_3^+ symmetric deformation in amino acids that were likely present in this sample (Suzuki *et al.* 1959, Pearson and Slifkin 1972). In other words, the spot that was sampled for spectrum slide 6a1 contained a somewhat different mixture of plasma, protein, and other substances than the one sampled in slide 6a2 and on the NaCl plate in transmission mode. The differences between the spectra are, therefore, clearly attributable to compositional differences rather than anything inherent in reflectance FTIRM spectrophotometry. This illustrates, again, the sensitivity of FTIRM to small compositional differences within a sample (the two spectra were obtained from different spots on the same drop of blood).

In Fig. 5, we present reflectance and transmission FTIRM spectra for feather barbules, compared with a standard for keratin (from a human fingernail) from the Kimmel Library (peak assignments are in Table 4). Note that the reflectance and transmission FTIRM spectra are nearly identical to each other. They are also similar

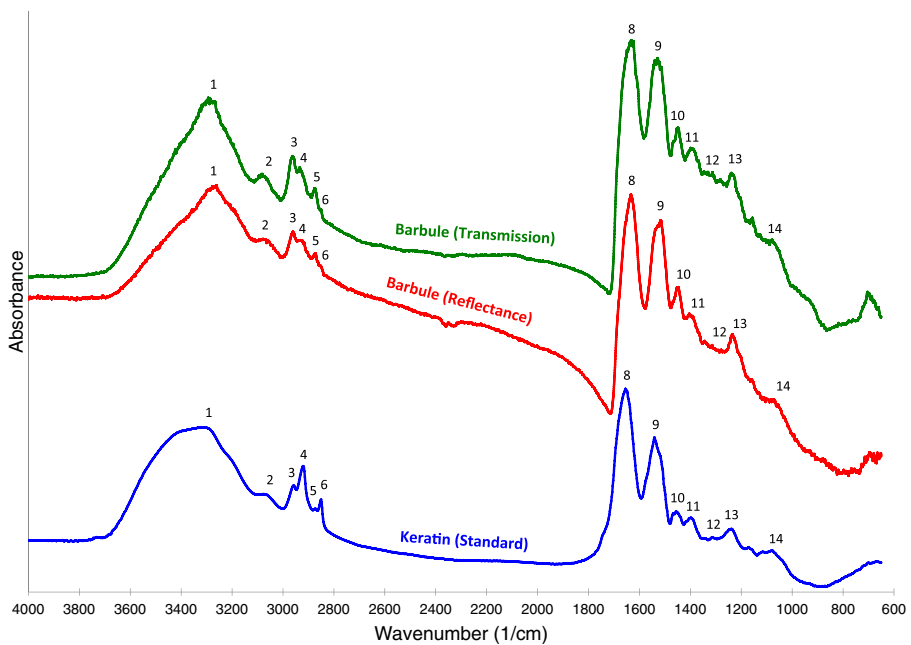


Fig. 5 FTIRM spectra of feather barbule residues obtained in reflectance mode (on a mirrored slide) and in transmission mode (on a NaCl plate), compared with an FTIR standard for keratin (prepared using the KBr pellet method) from the Kimmel Center for Archaeological Science, Weizmann Institute of Science. Peak assignments are in Table 4. The reflectance spectrum (*red line*) is nearly identical to the transmission spectrum (*green line*); both clearly exhibit the protein peaks seen in the keratin standard (*blue line*). The reflectance spectrum is graphed in calculated absorbance mode ($\log(1/R)$). Note that spectra are plotted on the same scale, but have been vertically offset.

to the keratin standard between 1700 and 1000 cm^{-1} , even though fingernails are composed of α -keratin, whereas feathers are composed of β -keratin. As with the other animal tissues examined in this study, such as skin, meat, and blood, feathers exhibit the amide A, B, I, II, and III peaks typical of protein, with smaller peaks from CHx bending vibrations present between the amide II and III bands (see Table 4).

The FTIRM spectra we obtained on the calamus of the feather are presented in Fig. S1. This figure shows, like the others, that it is possible to obtain an excellent reflectance FTIRM spectrum on this type of animal tissue. The reflectance and transmission FTIRM spectra are very similar to each other. They are also consistent with the Kimmel Library's keratin standard.

In Fig. 6, the reflectance and transmission FTIRM spectra for deer hair are presented, along with the same keratin standard used to assess the feather residue spectra. The reflectance spectrum is saturated (as can be seen by the noisy peaks; this is because reflectance was low); nevertheless, it is clear that it is consistent with the keratin standard. The transmission FTIRM spectrum, on the other hand, differs from both of these by the presence of an extremely strong peak centered on 1071 cm^{-1} (peak 14). This band is characteristic of the class of hair pigments known as pheomelanins (Kolczyńska-Szafranec and Bilińska 1993) and has been attributed to deformational vibration of the C-H groups of thiazole and benzothiazole systems (Rao and Venkataraghavan 1963). This particular hair sample, therefore, contains more pheomelanin than the sample on the

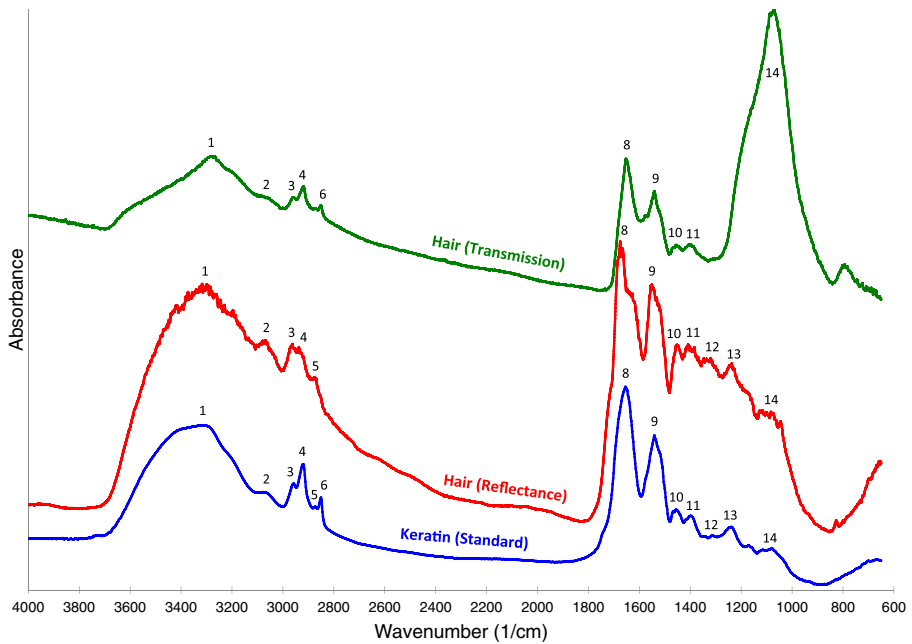


Fig. 6 FTIRM spectra of deer hair residues obtained in reflectance mode (on a mirrored slide) and in transmission mode (on a NaCl plate), compared with an FTIR standard for keratin (prepared using the KBr pellet method) from the Kimmel Center for Archaeological Science, Weizmann Institute of Science. Peak assignments are in Table 5. The reflectance spectrum (*red line*) is similar to the keratin standard (*blue line*). The transmission spectrum (*green line*) differs from both by the presence of a very strong peak at $\sim 1071\text{ cm}^{-1}$ (peak 14), attributed to the presence of pheomelanins in this sample. The reflectance spectrum is graphed in calculated absorbance mode ($\log(1/R)$). Note that spectra are plotted on the same scale, but have been vertically offset.

mirrored slide. We attribute this compositional difference to the fact that the samples for reflectance and transmission FTIRM for hair were prepared by different individuals, who likely sampled different hairs or different portions of the hair.

Figure 7 presents the reflectance and transmission FTIRM spectra for fresh beef bone, compared with a bone standard from the Kimmel Library (peak assignments are in Table 6). The reflectance spectrum is of excellent quality, like most of the other reflectance spectra. In terms of peak locations and intensities, both the transmission and reflectance FTIRM spectra are consistent with the goat bone FTIR spectrum from the Kimmel library. All three spectra exhibit the amide I, II, and III bands (at peaks 7, 8, and 11) typical of protein—in this case, collagen. The mineral content of the bone is evidenced in peaks 9, 10, and 15 (carbonate stretching) and 12–14 (phosphate stretching). The reflectance FTIRM spectrum differs from the other two in that the peak at 963 cm^{-1} (peak 14, assigned to PO_4 symmetric stretching), relatively weak in the transmission FTIRM spectrum and the goat bone, is so strong that it joins the peak at 1032 cm^{-1} (peak 13, assigned to PO_4 asymmetric stretching), resulting in a very strong, broad peak (possibly oversaturated) in the reflectance spectrum. The transmission spectrum is very similar to the reflectance spectrum; it is somewhat noisier, probably because insufficient light passed through the sample.

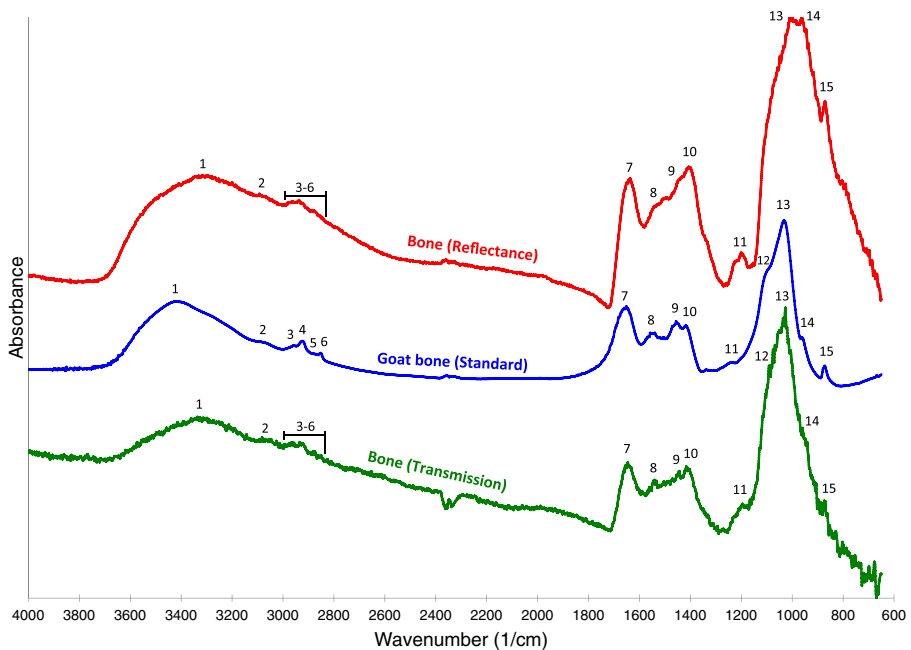


Fig. 7 FTIRM spectra of beef bone obtained in reflectance mode (on a mirrored slide; red line) and in transmission mode (on a NaCl plate; green line), compared with an FTIR standard for goat bone (prepared using the KBr pellet method) from the Kimmel Center for Archaeological Science, Weizmann Institute of Science. Note that the goat bone from the Kimmel standard was part of a burning experiment; it was described as “slightly burned” and assigned a “burn code” of 1 (Stiner *et al.* 1995; Weiner 2010:294). Nevertheless, this spectrum (blue line) is a good match for both of our FTIRM spectra. Peak assignments are in Table 6. The reflectance spectrum is graphed in calculated absorbance mode ($\log(1/R)$). Note that spectra are plotted on the same scale, but have been vertically offset.

In Fig. 8 (and Table 7), we present the FTIRM spectra of fish scales, which are dominated by an intense peak at $\sim 1040\text{ cm}^{-1}$ (peak 4). We attribute this band to phosphate (PO_4) stretching from the mineral hydroxyapatite, which composes the outer layer of fish scales, as noted earlier. We have included a standard for the mineral hydroxyapatite from the Kimmel Library for comparison; the location of the major absorption band for this sample is clearly consistent with that of the fish scales, although the hydroxyapatite standard has a more ordered atomic structure, as can be seen by the narrowness of the peak and the presence of additional, sharp peaks. The fish scale spectra also exhibit some protein peaks, as we would expect from the description of fish scale composition provided earlier, which can tentatively be attributed to amide I at $\sim 1650\text{ cm}^{-1}$ (peak 1) and amide II at $\sim 1530\text{ cm}^{-1}$ (peak 2). We attribute the weak peak at location #3 ($\sim 1422\text{ cm}^{-1}$) to carbonate (CO_3) stretching, and it is also visible, as a weak doublet, in the hydroxyapatite standard. Finally, it is worth noting that the quality of the reflectance spectrum is excellent—in fact, it has a greater signal-to-noise ratio than the transmission FTIRM spectrum because the latter transmitted a very low signal (perhaps the fish scale particles were too thick to easily transmit light).

Finally, in Fig. 9 (and Table 8), we present two reflectance FTIRM spectra and one transmission FTIRM spectrum for beef fat. As we did for meat and blood, in this figure, we endeavor to present some of the variability we found between different spots

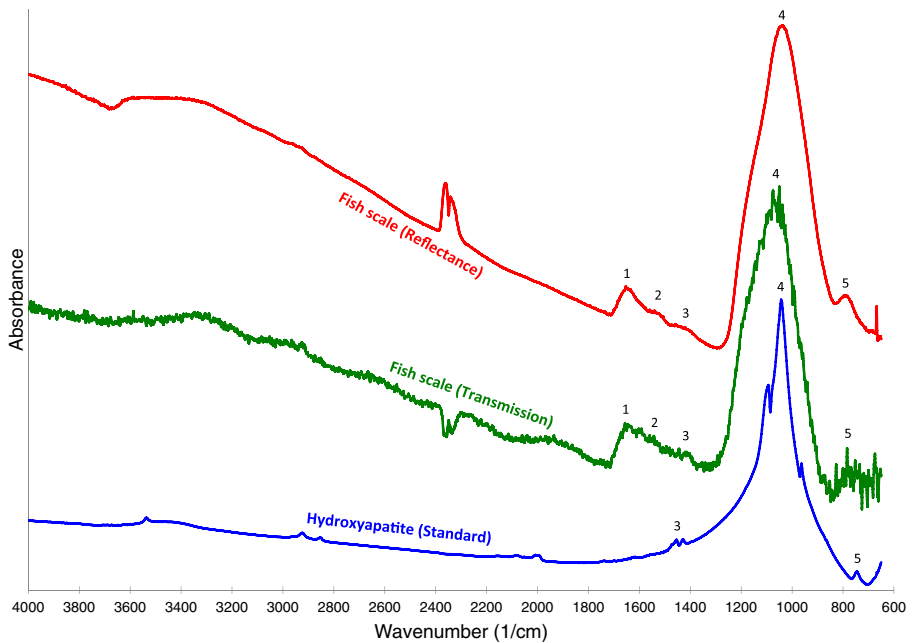


Fig. 8 FTIRM spectra of fish scale obtained in reflectance mode (on a mirrored slide; red line) and in transmission mode (on a NaCl plate; green line), compared with an FTIR standard for hydroxyapatite (prepared using the KBr pellet method) from the Kimmel Center for Archaeological Science, Weizmann Institute of Science (blue line). The fish scale reflectance and transmission spectra are identical, and clearly evidence the phosphate absorbance peak seen in the hydroxyapatite standard at $\sim 1040\text{ cm}^{-1}$ (peak 4). Peak assignments are in Table 7. The peaks on the reflectance and transmission spectra at $\sim 2350\text{ cm}^{-1}$ are due to atmospheric CO_2 and should be ignored. The reflectance spectrum is graphed in calculated absorbance mode ($\log(1/R)$). Note that spectra are plotted on the same scale, but have been vertically offset.

analyzed. Reflectance spectrum slide 6b3 is virtually identical to the FTIRM transmission spectrum. They both evidence CH_2 (especially) and CH_3 stretching vibrations between ~ 2950 and $\sim 2850\text{ cm}^{-1}$ (peaks 3–6), carbonyl stretching at 1743 cm^{-1} (peak 7), weak amide I and II bands (peaks 8 and 10, respectively), and a very strong band at $\sim 1025\text{ cm}^{-1}$ (peak 13) due to C-C and C-O stretching of the triglycerides which are the main constituent of intramuscular fat. The other reflectance FTIRM spectrum, slide 6b1, exhibits greater absorbance at peaks 1, 2, 8, and 10. These are the bands attributed to amide A, B, I, and II, respectively (see Table 8). Therefore, this spectrum comes from a spot that contains more protein than the other two spectra.

In sum, this experiment shows that reflectance FTIRM spectra for a wide range of animal tissues—skin, hair, feathers, fish scales, bones, meat, fat, and blood—can effectively be obtained when conditions are ideal (*i.e.*, using fresh samples that have been finely ground and placed on a highly reflective substrate). In addition to showing that these spectra are of excellent quality and are not affected by inverted or derivative bands, we show that they are consistent with the spectra of pure compounds (proteins and minerals) from the Kimmel library and that they therefore provide useful chemical and structural information. The reflectance FTIRM spectra that we describe above have been designated the reflectance FTIRM “standards” and will be referred to as such in the following section and on our web-based library (<http://z.umn.edu/ftir>).

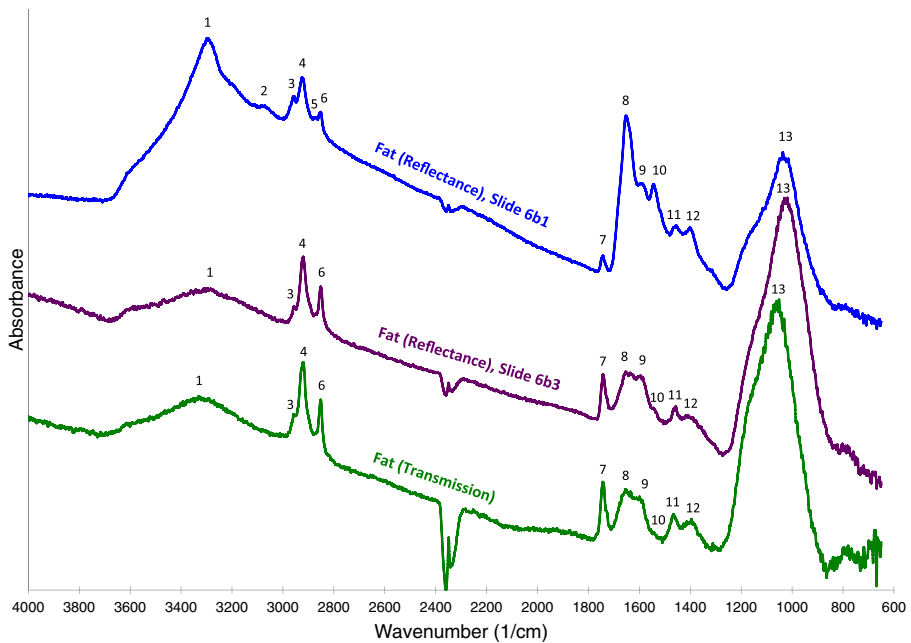


Fig. 9 FTIRM spectra for beef fat obtained in reflectance mode (on mirrored slides) and in transmission mode (on a NaCl plate). One of the reflectance spectra (purple line) is identical to the transmission spectrum (green line). Differences between the two reflectance spectra are attributable to differing relative amounts of protein in these two fat samples. Peak assignments are in Table 8. The peaks at $\sim 2350\text{ cm}^{-1}$ are due to atmospheric CO_2 and should be ignored. The reflectance spectra are graphed in calculated absorbance mode ($\log(1/R)$). Note that spectra are plotted on the same scale, but have been vertically offset.

Exploring the Effects of Stone Substrates on Residue Reflectance Spectra

One of the greatest challenges in developing a methodology of in situ reflectance FTIRM has been understanding and managing spectral interference from the stone (Cesaro and Lemorini 2012, Prinsloo *et al.* 2014, Solodenko *et al.* 2015). The problem stems from the fact that most stones that commonly serve to create tools, such as flint and obsidian, produce reflectance FTIRM spectra that are distorted relative to traditional transmission KBr pellet FTIR spectra. This led Prinsloo *et al.* (2014) to advocate developing a set of reference spectra for residues as well as for the stone substrates on which they occur. We have answered this call not only by developing reference reflectance spectra for plant (Monnier *et al.* 2017) and animal residues (this paper) and for common toolstone materials but also by systematically examining the nature of reflectance FTIRM spectra for each residue type on stone substrates. Therefore, after having obtained reflectance spectra for each of our residue slurries on the mirrored slides, we created another set of residue slurries that we deposited on stone flakes (obsidian, English flint, dacite, and Texas chert), using the methods described earlier. The description of our results follows, focusing mainly on obsidian and flint, with peak assignments presented in Tables 1, 2, 3, 4, 5, 6, 7, and 8 and spectra illustrated in Figs. 10, 11, 12, 13, 14, 15, 16, and 17.

To describe the effect(s) of the stone substrates on the residue spectra, we first depict, on the same scale, a reflectance spectrum for English flint by itself (blue line, Fig. 10)

Table 1 Infrared absorption bands and proposed assignments for skin spectra presented in Figs. 2, 11, 12, and 13

Sample type:	Collagen	Sample substrate:	KBr pellet	Al-coated slide	NaCl plate	Flint	Obsidian
Spectrum title:	Collagen (pure, fresh)	Slide 10a2	Plate 10a_04122016b				*OBS_10a_1a
Instrument:	FTIR spectrometer, Weizmann	FTIR microscope, reflectance mode	FTIR microscope, transmittance mode				FTIR microscope, reflectance mode
Correction:	None	None	None				Kramers-Kronig
Figures:	Figure 2, blue line	Fig. 2, red line; Figs. 11 and S2, purple line	Fig. 2, green line				Fig. S2, blue line
	Absorption band	Proposed assignment	Peak #	Absorption band	Absorption band	Absorption band	Absorption band
	3412 (vs)	O-H stretching, amide A	1	3299 (s)	3318 (s)	3303	3285
	3085 (s)	amide B	2	3070 (m)	3084 (m)	3084	-
	2957 (m)	CH ₃ asymmetric stretching	3	2959 (sh)	2958 (sh)	2962	2959
	-	CH ₂ asymmetric stretching	4	2924 (vs)	2925 (vs)	2922	2922
	2880 (m)	CH ₃ symmetric stretching	5	-	-	-	-
	-	CH ₂ symmetric stretching	6	2854 (s)	2853 (s)	2849	2851
	-	C = O stretching	7	1746 (m)	1745 (s)	1736	1737
	1658 (s)	Amide I	8	1671 (vs)	1655 (vs)	1655	1658
	1548 (s)	Amide II	9	1555 (s)	1544 (s)	1538	1540
	1454 (s)	CH _x bending	10	1456 (s)	1455 (m)	1446	1453

Table 2 Infrared absorption bands and proposed assignments for meat spectra presented in Figs. 3 and 12

Sample type:	Meat (beef)		
Sample substrate:	Al-coated slide	NaCl plate	
Spectrum title:	Slide 1a-j	Plate 1 h	
Instrument:	FTIR microscope, reflectance mode	FTIR microscope, transmittance mode	
Correction:	None	None	
Figures:	Figure 3, blue line	Fig. 3, green line	
	Obsidian	Dacite	*OBS_1a_1f
	FTIR microscope, reflectance mode	FTIR microscope, reflectance mode	FTIR microscope, reflectance mode
	None	None	Kramers-Kronig
	Figure 3, blue line	Fig. 3, green line	Fig. 12, blue line
	Proposed assignment	Absorption band	Absorption band
	band	band	band
	3292 (s)	3284 (s)	3299
	Amide A	3062 (s)	3078
	3072 (m)	2961 (s)	2962
	Amide B	2931 (s)	2934
	CH ₃ asymmetric stretching	2873 (m)	2875
	2925 (m)	2853 (m)	2854
	CH ₂ asymmetric stretching	1742 (w)	—
	2873 (m)	1653 (vs)	1657
	CH ₃ symmetric stretching	1625 (vs)	—
	2853 (m)	1546 (s)	—
	CH ₂ symmetric stretching	1456 (m)	1548
	1742 (w)	1395 (s)	1455
	C = O stretching	—	1383
	1653 (vs)	—	—
	C = C stretching, amide I	—	—
	1625 (vs)	—	—
	Amide I	—	—
	1546 (s)	—	—
	Amide II	—	—
	1456 (m)	—	—
	CH _x bending	—	—
	1395 (s)	—	—
	CH _x bending	—	—

Table 2 (continued)

Sample type:	Meat (beef)	Meat (beef)	NaCl plate	Dacite	Obsidian
Sample substrate:	Al-coated slide	Al-coated slide			
Spectrum title:	Slide la-j	Slide la-l	Plate 1 h	*DAC_1a_2a	*OBS_1a_1f
Instrument:	FTIR microscope, reflectance mode	FTIR microscope, reflectance mode	FTIR microscope, transmittance mode	FTIR microscope, reflectance mode	FTIR microscope, reflectance mode
Correction:	None	None	None	Kramers-Kronig	Kramers-Kronig
Figures:	Figure 3, blue line	Fig. 3, purple line; Fig. 12, red line	Fig. 3, green line	Fig. 12, green line	Fig. 12, blue line
	1306 (m)	1308 (m)	1303 (s)	n/a	n/a
	1241 (m)	1241 (m)	1241 (s)	n/a	n/a
	1161 (m)	1164 (m)	1168 (m)	n/a	n/a
	1113 (m)	C-N, C-C stretching	1087 (m)	n/a	n/a
	982 (m)	=C-H out of plane bending	972 (m)	n/a	n/a

The * symbol occurring at the beginning of a spectrum title signifies that the spectrum has been corrected using the Kramers-Kronig correction

Vibrational mode assignments are based upon Calabrò and Magazu *et al.* 1958, Jung 2000, and Barth 2007. Letters after wavenumbers indicate band intensity vs very strong, *s* strong, *m* medium, *sh* shoulder, *w* weak

Table 3 Infrared absorption bands and proposed assignments for blood spectra presented in Figs. 4 and 13

Sample type:	Blood (beef)	Blood (beef)	NaCl plate	Flint	Obsidian
Sample substrate:	Al-coated slide	Al-coated slide	Plate 6a3	*EFL_6a_1d	*OBS_6a_2b
Spectrum title:	Slide 6a1	Slide 6a2			
Instrument:	FTIR microscope, reflectance mode	FTIR microscope, reflectance mode	FTIR microscope, transmittance mode	FTIR microscope, reflectance mode	FTIR microscope, reflectance mode
Correction:	None	None	None	Kramers-Kronig	Kramers-Kronig
Figures:	Figure 4, blue line	Fig. 4, purple line; Fig. 13, red line	Fig. 4, green line	Fig. 13, green line	Fig. 13, blue line
	Absorption band	Absorption band	Absorption band	Absorption band	Absorption band
	Proposed assignment	Proposed assignment			
	Peak #	Peak #			
	3306 (s)	1 3291 (vs)	3302 (s)	3296	3299
	3061 (m)	2 3056 (m)	3063 (m)	3061	3070
	2958 (s)	3 2958 (m)	2959 (m)	2961	2961
	2937 (s)	4 2937 (m)	2936 (m)	2931	2936
	2872 (s)	5 2873 (w)	2872 (m)	2870	2875
	1679 (vs)	6 1661 (vs)	1656 (vs)	1658	1658
	1599 (vs)	7 -	-	-	-
	1551 (s)	8 1544 (s)	1543 (s)	1544	1542
	1503 (vs)	9 -	-	-	-
	1454 (m)	10 1454 (m)	1455 (w)	1454	1456
	1392 (m)	11 1395 (m)	1396 (w)	1387	1389
	1306 (m)	12 1308 (m)	1310 (w)	1300	-

Table 3 (continued)

Sample type:	Blood (beef)	Blood (beef)			
Sample substrate:	Al-coated slide	Al-coated slide	NaCl plate	Flint	Obsidian
Spectrum title:	Slide 6a1	Slide 6a2	Plate 6a3	*EFL_6a_1d	*OBS_6a_2b
Instrument:	FTIR microscope, reflectance mode	FTIR microscope, reflectance mode	FTIR microscope, transmittance mode	FTIR microscope, reflectance mode	FTIR microscope, reflectance mode
Correction:	None	None	None	Kramers-Kronig	Kramers-Kronig
Figures:	Figure 4, blue line	Fig. 4, purple line; Fig. 13, red line	Fig. 4, green line	Fig. 13, green line	Fig. 13, blue line
	1236 (m)	1229 (m)	1239 (w)	—	—
	1104 (s)	1079 (s)	1081 (m)	—	—
	Amide III				
	C-O, C-C, C-N,				
	P = O stretching				

The * symbol occurring at the beginning of a spectrum title signifies that the spectrum has been corrected using the Kramers-Kronig correction

Vibrational mode assignments are based upon Deléris and Petitbois 2003, Miyazawa *et al.* 1958, Suzuki *et al.* 1959, Pearson & Sifkin 1972, Jung 2000, and Barth 2007. Letters after wavenumbers indicate band intensity

vs very strong, *s* strong, *m* medium, *sh* shoulder, *w* weak

Table 4 Infrared absorption bands and proposed assignments for feather spectra presented in Figs. 5, 14, S1, and S3

Sample type:	Sample substrate:	Spectrum title:	Instrument:	Correction:	Figures:	Feather barbule				Feather calamus				
						Al-coated slide	NaCl plate	Obsidian	English flint	Al-coated slide	NaCl plate	Obsidian	English flint	
Keratin	KBr pellet	Keratin (fingernail)	FTIR spectrometer, Weizmann	None	Figs. 5 and S1; blue line	Slide 4a1	Plate 4a11	OBS_4a_1b	EFL_4a_1b	Slide 4b2	Plate 4b2	OBS_4b_2b	EFL_4b_1b	
						FTIR microscope, reflectance mode	FTIR microscope, transmittance mode	FTIR microscope, reflectance mode	FTIR microscope, reflectance mode	FTIR microscope, reflectance mode	FTIR microscope, transmittance mode	FTIR microscope, reflectance mode	FTIR microscope, reflectance mode	FTIR microscope, reflectance mode
						None	None	None	None	None	None	None	None	None
						Figs. 5 and 14, red line	Fig. 5, green line	Fig. 14, blue line	Fig. 14, green line	Figs. S1 and S3, red line	Fig. S1, green line	Fig. S3, green line	Fig. S3, blue line	Fig. S3, blue line
						Absorption band	Absorption band	Absorption band	Absorption band	Absorption band	Absorption band	Absorption band	Absorption band	Absorption band
						Peak #								
						Proposed assignment								
						3309 (s) Amide A	3261 (s)	3293	3345	3301 (s)	3311 (s)	3289	3304	
						3075 (m) Amide B	3078 (m)	3081	-	3075 (m)	3080 (m)	3070	3082	
						2958 (m) CH ₃ asymmetric stretching	2963 (m)	2961	2966	2961 (m)	2964 (m)	2961	2966	
						2921 (m) CH ₂ asymmetric stretching	2934 (m)	2936	2931	2923 (s)	2924 (m)	2932	2934	
						2873 (m) CH ₃ symmetric stretching	2875 (m)	2878	-	2873 (m)	2876 (w)	2872	2880	
						2851 (m) CH ₂ symmetric stretching	2854 (sh)	-	-	2851 (m)	2853 (m)	2857	-	
						C=O stretching	-	-	-	1741	1742 (w)	-	-	
						1655 (vs) Amide I	1632 (s)	1670	1690	1637 (vs)	1654 (vs)	1664	1691	
						1541 (s) Amide II	1528 (s)	1549	1561	1541 (s)	1546 (s)	1557	1559	
						1455 (m) CH _x bending	1449 (m)	1457	1450	1450 (m)	1456 (m)	1458	1459	
						1397 (m) CH _x bending	1398 (m)	1397	1393	1405 (m)	1403 (m)	1397	1405	

Table 5 (continued)

Sample type:	Keratin	Hair (deer)			
Sample substrate:	KBr pellet	Al-coated slide	NaCl plate	Obsidian	English flint
Spectrum title:	Keratin (fingernail)	Slide 7b3	Plate 7b_04122016b	OBS_7b_1b	EFL_7b_1b
Instrument:	FTIR spectrometer, Weizmann	FTIR microscope, reflectance mode	FTIR microscope, transmittance mode	FTIR microscope, reflectance mode	FTIR microscope, reflectance mode
Correction:	None	None	None	None	None
Figures:	Fig. 6, blue line	Figs. 6 and 15, red line	Fig. 6, green line	Fig. 15, green line	Fig. 15, blue line
	1238 (m) Amide III	13	1237 (m)	—	—
	1080 (w) C-N, C-C stretching	14	1083 (m)	1071 (vs)	1047

Vibrational mode assignments are based upon Rao and Venkataraghavan 1963, Baddiel 1968, Jung 2000, and Barth 2007. Letters after wavenumbers indicate band intensity vs very strong, *s* strong, *m* medium, *sh* shoulder, *w* weak

Table 6 Infrared absorption bands and proposed assignments for bone spectra presented in Fig. 7

Sample type:	Bone (goat)	Bone (beef)
Sample substrate:	KBr pellet	Mirror-coated slide
Spectrum title:	Bone burnt Goat Burn = 1	Slide 9a1
Instrument:	FTIR spectrometer, Weizmann	FTIR microscope, reflectance mode
Correction:	None	None
Figures:	Figure 7, blue line	Fig. 7, red line
	Absorption band	Absorption band
	3416 (s)	3299 (s)
	3076 (m)	3074 (m)
	2957 (m)	2980–2840 (m)
	2924 (m)	2980–2840 (m)
	2878 (m)	2980–2840 (m)
	2852 (m)	2980–2840 (m)
	1651 (s)	1636 (s)
	1553 (m)	1543 (sh)
	1455 (m)	1452 (sh)
	1417 (m)	1406 (s)
	1238 (w)	1226 (w)
	1105 (sh)	–
	1032 (vs)	1009 (vs)
	961 (sh)	963 (vs)
	872 (w)	871 (sh)
		875
	Proposed assignment	Peak #
	Amide A	1
	Amide B	2
	CH ₃ asymmetric stretching	3
	CH ₂ asymmetric stretching	4
	CH ₃ symmetric stretching	5
	CH ₂ symmetric stretching	6
	Amide I	7
	Amide II	8
	CO ₃ asymmetric stretching, CH _x bending	9
	CO ₃ symmetric stretching, CH _x bending	10
	Amide III	11
	PO ₄ asymmetric stretching	12
	PO ₄ asymmetric stretching	13
	PO ₄ symmetric stretching	14
	CO ₃ asymmetric deformation	15

Vibrational mode assignments are based upon Fowler 1974 and Rehman and Bonfield 1997. Letters after wavenumbers indicate band intensity

vs very strong, s strong, m medium, sh shoulder, w weak

Table 7 Infrared absorption bands and proposed assignments for fish scale spectra presented in Figs. 9 and 19

Sample		Fish scale			
type:	Hydroxyapatite				
Sample substrate:	KBr pellet	Al-coated slide	NaCl plate	Flint	Obsidian
Spectrum title:	Apatite (wards)	Slide 9b2	Plate 9b2	EFL_9b_1a	OBS_9b_2a
Instrument:	FTIR spectrometer, Weizmann	FTIR microscope, reflectance mode	FTIR microscope, transmittance mode	FTIR microscope, reflectance mode	FTIR microscope, reflectance mode
Correction:	None	None	None	None	None
Figures:	Figure 8, blue line	Figs. 8 and 16, red line	Fig. 8, green line	Fig. 16, blue line	Fig. 16, green line
	Absorption band (hydroxyapatite)	Absorption band	Absorption band	Absorption band	Absorption band
	Proposed assignment	Peak #			
	Amide I	1	1653 (w)	1704/1688	1676
	Amide II	2	1531 (w)	1590/1578	1578/1557
	CO ₃ asymmetric stretching	3	1422 (w)	1465/1416	1467/1422
	PO ₄ asymmetric stretching	4	1039 (vs)	–	–

Vibrational mode assignments are based upon Ikoma *et al.* 2003. Letters after wavenumbers indicate band intensity

vs very strong, *s* strong, *m* medium, *sh* shoulder, *w* weak

Table 8 Infrared absorption bands and proposed assignments for fat spectra presented in Figs. 9 and 17

Sample type:	Fat (beef)	Fat (beef)	NaCl plate	Flint	Obsidian
Sample substrate:	Al-coated slide	Al-coated slide	NaCl plate	Flint	Obsidian
Spectrum title:	Slide 6b1	Slide 6b3	Plate 6b3	EFL_6b_1b	*OBS_6b_1c
Instrument:	FTIR microscope, reflectance mode	FTIR microscope, reflectance mode	FTIR microscope, transmittance mode	FTIR microscope, reflectance mode	FTIR microscope, reflectance mode
Correction:	None	None	None	None	Kramers-Kronig
Figures:	Fig. 9, blue line	Fig. 9, purple line; Fig. 17, red line	Fig. 9, green line	Fig. 17, blue line	Fig. 17, green line
	Absorption band	Proposed assignment	Peak #	Absorption band	Absorption band
	3300 (s)	O-H stretching, amide A	1	3300 (m)	—
	3073 (s)	Amide B	2	—	—
	2957 (s)	CH ₃ asymmetric stretching	3	2957 (m)	—
	2925 (s)	CH ₂ asymmetric stretching	4	2920 (s)	2920
	2875 (s)	CH ₃ symmetric stretching	5	—	—
	2852 (s)	CH ₂ symmetric stretching	6	2851 (s)	2852
	1744 (w)	C = O stretching	7	1743 (m)	1742
	1652 (s)	Amide I	8	1653 (m)	—
	1591 (m)	Possibly asymmetric C(O)O stretching	9	1600 (m)	—
	1544 (m)	Amide II	10	1544 (sh)	—
	1456 (w)	CH ₂ bending	11	1457 (w)	1455
	1402 (w)	CH ₂ bending	12	1414 (w)	1411
	1029 (s)	C-O, C-C stretching	13	1025 (vs)	—

The * symbol occurring at the beginning of a spectrum title signifies that the spectrum has been corrected using the Kramers-Kronig correction. Vibrational mode assignments are based upon Vlachos *et al.* 2006 and Rahmania 2015. Letters after wavenumbers indicate band intensity vs very strong, s strong, m medium, sh shoulder, w weak

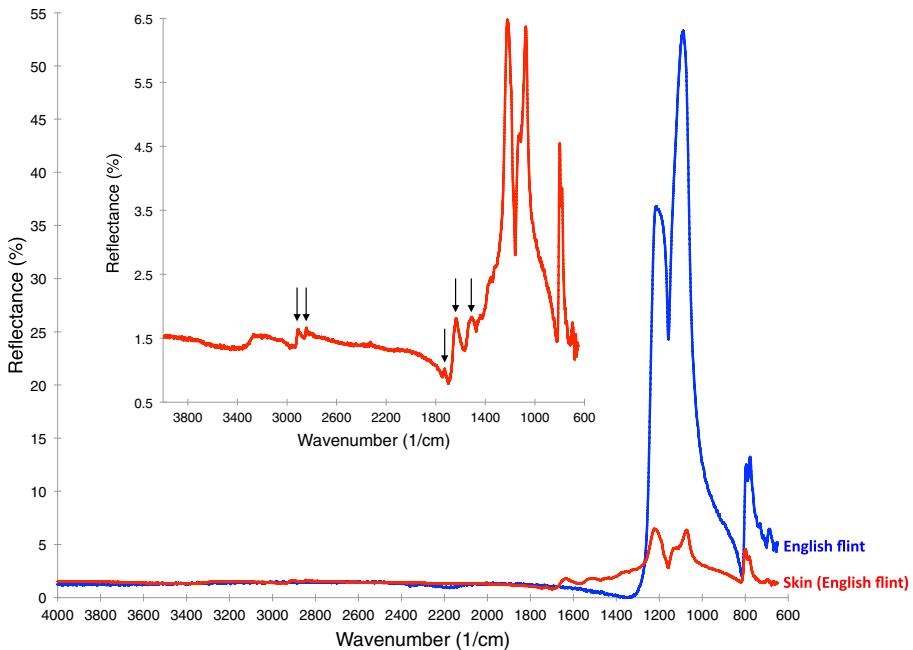


Fig. 10 FTIR reflectance spectra of English flint (*blue line*), and skin residue on English flint (*red line*), illustrated in reflectance mode rather than absorbance mode. In the main graph, these spectra are at the same scale relative to each other. The flint (*blue line*) exhibits almost no reflectance across most of the IR spectrum; however, between 1300 and 900 cm^{-1} , it exhibits a strong reststrahlen band. The skin residue on flint spectrum (*red line*) is weak, and is dominated by the signal from the flint (note how closely it mimics the flint spectrum). The *upper graph* shows the same skin residue on flint, illustrated on a larger scale so that the peaks are more apparent; the peaks highlighted by *arrows* are derivative peaks produced by specular reflection from the skin residue

and one for our skin residue on an English flint flake (red line, Fig. 10). We present these spectra in reflectance mode (%R, as used by Prinsloo *et al.* 2014, Solodenko *et al.* 2015, and Zupancich *et al.* 2016) rather than absorbance mode (used for all of the other spectra in this paper), in order to discuss degree of reflectance. Note that the skin residue spectrum, although much lower in intensity, largely mimics the flint spectrum. It is also extremely distorted, relative to the skin residue reflectance standard (Fig. 11, purple line). There are two main and overlapping factors behind these distortions: the nature of reflectance from the surface of the skin residue, and the nature of reflectance from the stone. Recall that when the skin residue is located on a mirrored slide, the resulting spectrum is similar to an absorbance spectrum for collagen (with some differences indicating that our skin residue is not composed of pure collagen). The reason why the reflectance spectrum for skin on the mirrored slide is so good is because the Al coating of our mirrored slides reflects nearly 100% of light at all IR wavelengths. While some light is reflected from the surface of the skin residue, most of it passes through the residue, is reflected from the aluminum coating underneath it, and passes through the residue again, before returning to the detector. Therefore, the resulting spectrum shows that light of certain wavelengths has been absorbed by the residue, producing the absorbance peaks that we see. On the other hand, flint is not a

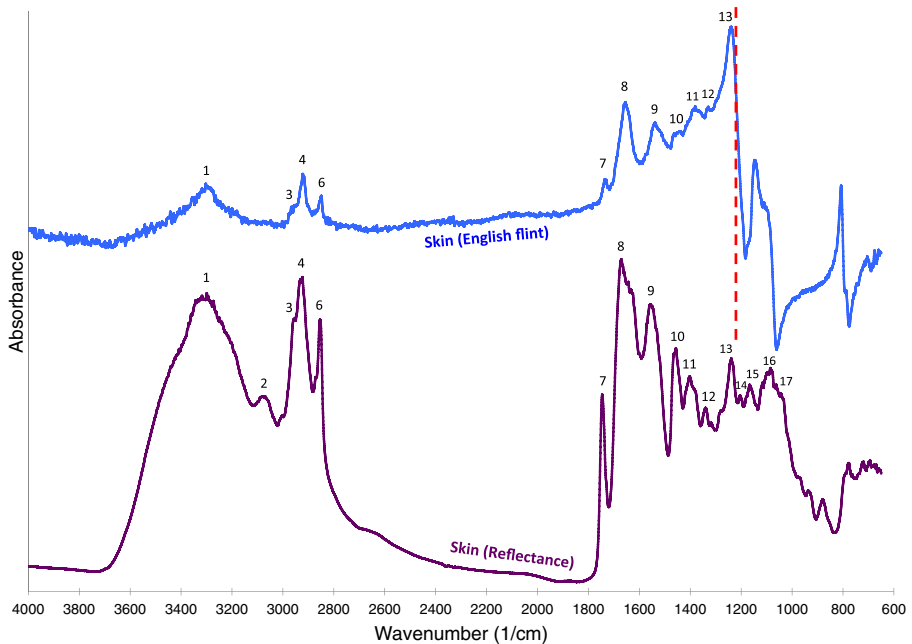


Fig. 11 The spectrum of skin on flint from Fig. 10 is presented here again (blue line), but with the Kramers-Kronig correction applied, and hence in absorbance mode. Comparison with the skin reflectance standard purple line shows that it exhibits recognizable peaks above 1250 cm^{-1} , although relative peak heights as well as the baseline are distorted. Below 1250 cm^{-1} , (to the right of the dashed line), the spectrum exhibits severe derivative peaks. Peak assignments are in Table 1. The reflectance standard (purple line) is graphed in calculated absorbance mode ($\log(1/R)$). Note that spectra are plotted on the same scale, but have been vertically offset.

good reflector. As shown in Fig. 10 (blue line), flint reflects less than 2% of light between ~ 4000 and 1300 cm^{-1} , at which point a band (called *reststrahlen*) of much higher reflection (30–55%) begins, abruptly ending at $\sim 1000\text{ cm}^{-1}$. Regarding the skin residue on flint, in the range where flint reflects almost no light ($4000\text{--}1300\text{ cm}^{-1}$), the only light returning to the detector is the light that has been reflected from the surface of the skin residue. Since this particular residue reflects light like a mirror (we call this specular reflection), this produces derivative bands in this region of the spectrum (Fig. 10, inset; this type of reflectance was also extensively noted by Prinsloo *et al.* 2014). Fortunately, application of the Kramers-Kronig correction transforms this derivative spectrum to one (Fig. 11, blue line) that is comparable with the skin residue reflectance standard (Fig. 11, purple line). Although the shape of the corrected spectrum is different from the standard, and the peaks in the range from 1750 to 1200 cm^{-1} are shifted along the X-axis by 5–15 wavenumbers (compare peak locations in Table 1), the Kramers-Kronig algorithm nevertheless currently stands as the best way to correct a spectrum produced by specular reflection. Unfortunately, no corrections can eliminate the derivative bands in the spectral region below 1200 cm^{-1} which are due to the IR signal from the flint. The dashed red line at 1200 cm^{-1} marks the location on the spectrum where the *reststrahlen* band from the flint appears, and below which the spectrum is no longer interpretable due to multiple derivative bands from the stone. Many of the same patterns are apparent in a reflectance spectrum of skin residue on an obsidian flake illustrated in Fig. S2.

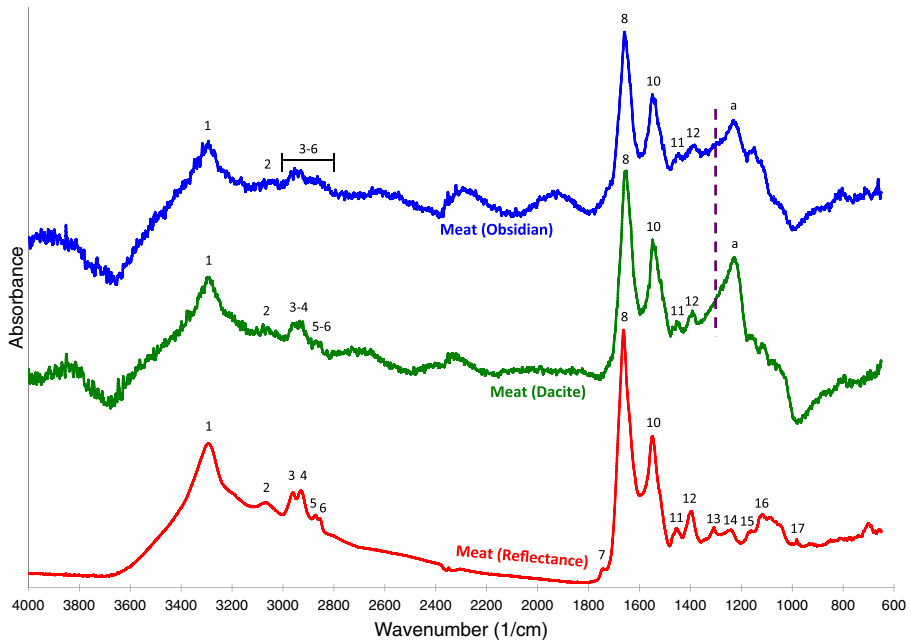


Fig. 12 FTIRM spectra (Kramers-Kronig corrected) for meat residue on obsidian and dacite, which show good correspondence with the meat reflectance standard above 1300 cm^{-1} . The peaks at location “a” are thought to be derivative peaks due to the stones’ reststrahlen band; we suggest that the spectra should not be used below 1300 cm^{-1} (to the right of the *dashed line*). Peak assignments are in Table 2. The reflectance standard (*red line*) is graphed in calculated absorbance mode ($\log(1/R)$). Note that spectra are plotted on the same scale, but have been vertically offset.

Figure 12 illustrates Kramers-Kronig-corrected spectra for meat residue on dacite and obsidian compared to the meat reflectance standard (for the meat residue on English flint, we invite readers to consult our website). We note that the reststrahlen effect from the flint is less severe than on the skin residues, as can be seen in the region below 1300 cm^{-1} . The difference in the peak shapes at location “a” ($\sim 1275\text{ cm}^{-1}$) compared with peaks 13 and 14 in the standard is difficult to interpret: is it a result of the flint’s reststrahlen band, or of compositional differences between the meat samples used on the stones versus those used on the mirrored slide? Another feature not present in the standard is a sinusoidal wave in the baseline between ~ 2800 and 1800 cm^{-1} , an artifact of specular reflectance (note: the same feature is present in Fig. S2). Fortunately, since few organic molecules absorb energy in this portion of the spectra, this is not a confounding issue. Despite the distortions, vibrational modes can be assigned to the meat on stone spectra depicted in this figure (see Table 2), which are consistent with the amide A and B peaks at ~ 3293 and 3074 cm^{-1} (peaks 1 and 2), as well as the CH_x stretching peaks between 2960 and 2850 cm^{-1} (peaks 3–6). The peaks between ~ 1800 and 1300 cm^{-1} are an excellent match for the reference spectrum, clearly exhibiting the amide I (peak 8) and II (peak 10) and CH_x bending peaks (peaks 11 and 12). Below 1300 cm^{-1} , the meat spectra are more difficult to interpret.

Figure 13 illustrates the Kramers-Kronig-corrected spectra for blood residues on obsidian and flint. These spectra exhibit peaks consistent with the blood reflectance standard: the amide A and B peaks (peaks 1 and 2; see Table 3), the CH_x stretching

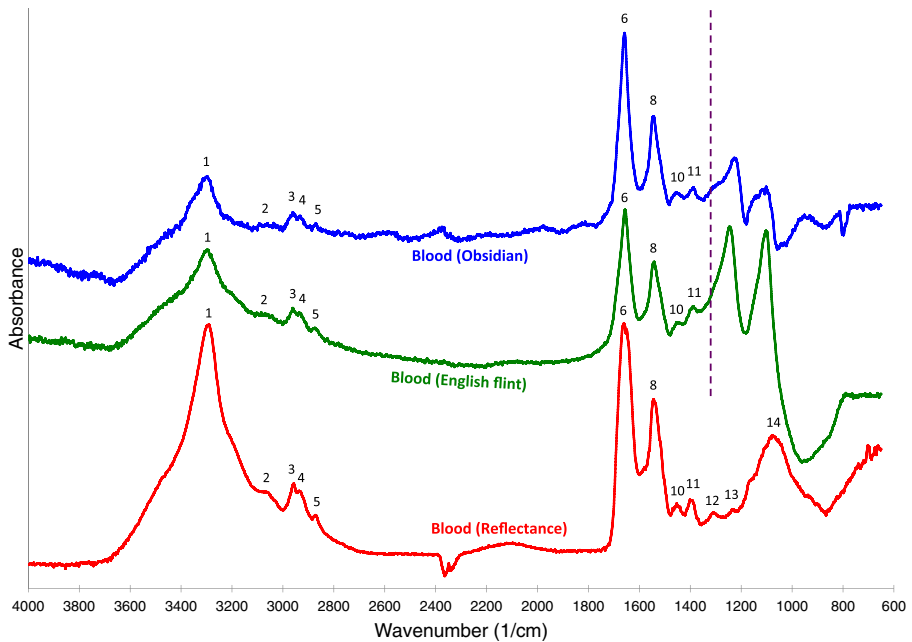


Fig. 13 FTIRM spectra (Kramers-Kronig corrected) for blood residue on obsidian and flint are consistent with the blood reflectance standard above 1300 cm^{-1} . Below that wavenumber (to the right of the *dashed line*), the spectra are strongly affected by derivative bands, which nevertheless seem to evidence absorbance at $\sim 1080\text{ cm}^{-1}$ (the location of peak 14), corresponding to a strong absorption band in our blood reflectance standard. Peak assignments are in Table 3. The reflectance standard (*red line*) is graphed in calculated absorbance mode ($\log(1/R)$). Note that spectra are plotted on the same scale, but have been vertically offset.

peaks (3–5), the amide I (peak 6) and amide II (peak 8) bands, as well as the CH_x bending peaks (10 and 11). Below 1350 cm^{-1} , the spectra are distorted due to the derivative bands in the flint and the obsidian, precluding direct comparison with the reflectance standard in the interval $\sim 1350\text{--}650\text{ cm}^{-1}$.

Our spectra for feather barbule residues on stone (Fig. 14) did not require the Kramers-Kronig correction, indicating that they are the result of diffuse, rather than specular, reflection. However, the results for the two stone substrates are very different. The spectrum that we collected for feather barbule residue on English flint is dramatically affected by the stone, as can be discerned by the strong drop in intensity at 1350 cm^{-1} , due to the flint's reststrahlen band. Despite this, peaks consistent with protein can be discerned above 1350 cm^{-1} (amide A at 3345 cm^{-1} , CH_x stretching at 2966 and 2931 cm^{-1} , amide I at $\sim 1690\text{ cm}^{-1}$, amide II at $\sim 1561\text{ cm}^{-1}$, and CH_x bending $\sim 1450\text{--}1350\text{ cm}^{-1}$; see also Table 4). On the other hand, the spectrum for feather barbules on obsidian is excellent. It exhibits all of the peaks present in the feather barbule residue reference standard, although some peaks are shifted up by 10–30 wavenumbers (the same is true of the spectrum on flint). Surprisingly, this spectrum does not display a reststrahlen band at 1300 cm^{-1} . This must mean that the spot measured for this spectrum had a dense enough residue that there is no contribution from the obsidian. In Fig. S3, we depict spectra obtained from feather calamus residues on flint and obsidian flakes. This time the residue on flint yielded a better spectrum than

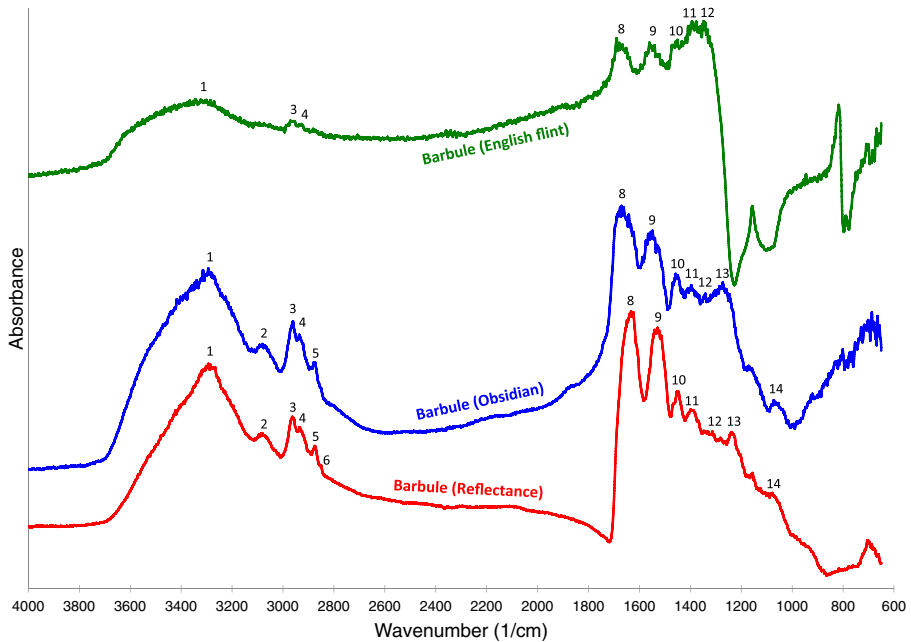


Fig. 14 The FTIR spectrum for feather barbule residue on English flint is distorted due to the flint's reststrahlen effect at $\sim 1300\text{ cm}^{-1}$. The FTIR spectrum for feather barbule residue on obsidian, on the other hand, is similar to the reflectance standard, although the locations of peaks 8–13 are shifted to higher wavenumbers. Peak assignments are in Table 4. All spectra are graphed in calculated absorbance mode ($\log(1/R)$). Note that spectra are plotted on the same scale, but have been vertically offset.

the residue on obsidian. This shows that the quality of the spectra depends less on the type of stone that is the substrate, and more on the nature of the residue itself.

The spectra for hair residue on stone substrates are presented in Fig. 15. Both spectra exhibit the same suite of peaks seen in the hair reflectance standard above 1350 cm^{-1} (see Table 5). Below that number, they are both primarily dominated by the stone reflectance spectrum.

The spectra for bone residue on stone substrates were saturated, with low signal-to-noise ratio and poor peak resolution. Therefore, they are not shown here but can be viewed at www.z.umn.edu/ftir.

The spectra for fish scale residues on stone (Fig. 16) also suffer from saturation of the detector and a low signal-to-noise ratio. While peaks between ~ 1700 and 1350 cm^{-1} consistent with the protein component of fish scale can be identified, the main hydroxyapatite peak at 1040 cm^{-1} is unfortunately lost due to the flint and obsidian's reststrahlen bands at 1300 – 1000 cm^{-1} .

Finally, the fat residues on stone (Fig. 17) show the same patterning seen in many of the other residues. First, the spectrum of fat residue on obsidian requires the Kramers-Kronig correction (the spectrum of fat residue on flint does not). Second, the peak shapes and locations for these spectra are comparable to those of the fat reflectance standard. The spectra exhibit sharp peaks for CH_2 stretching (peaks 4 and 6) and CH_x bending (peaks 11 and 12) as well as for $\text{C}=\text{O}$ stretching (peak 7), all of which are consistent with a high proportion of fatty acids. While the reflectance standard (red line)

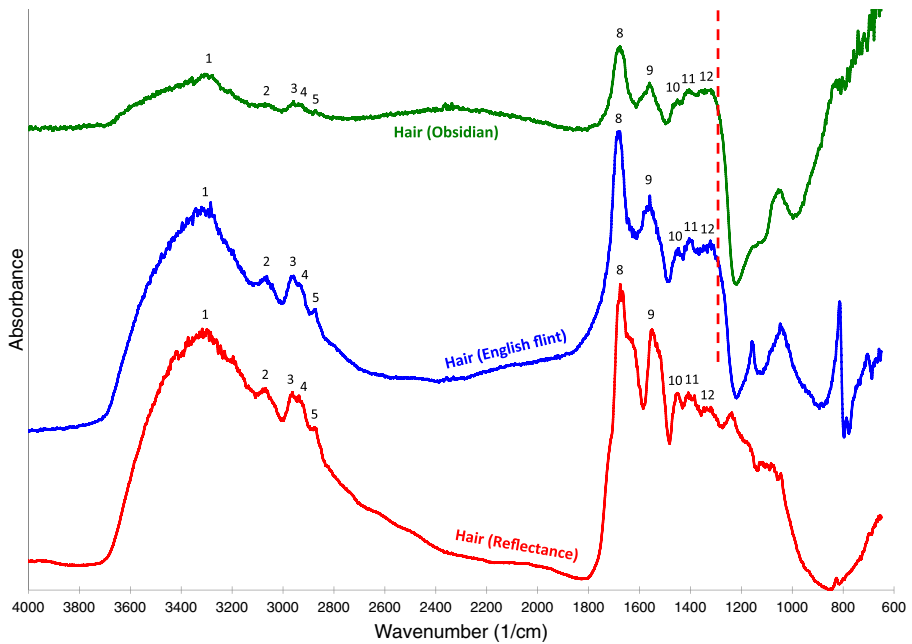


Fig. 15 The FTIRM spectra for deer hair residue on English flint and obsidian compared with the hair reflectance standard. The residues on obsidian and flint evidence peak shifts (for peaks 8–12) to higher wavenumbers, relative to the standard (*red line*); both also exhibit derivative bands below 1300 cm^{-1} (to the right of the *dashed line*). Peak assignments are in Table 5. All spectra are graphed in calculated absorbance mode ($\log(1/R)$). Note that spectra are plotted on the same scale, but have been vertically offset.

contains some moderate-sized protein peaks (peaks 8–10) not seen in the spectra of fat residue on stone, their absence is likely due to compositional differences between the samples, which were prepared at different times by different individuals (*i.e.*, the person who prepared the fat residue for the reflectance standard likely used a piece of fat that contained some meat). Below 1350 cm^{-1} , both residues on stone spectra are badly affected by derivative bands.

Discussion

Our data show that reflectance FTIRM spectra of animal-tissue residues placed on an ideal substrate, such as Al-coated slides, are nearly identical to the transmission FTIRM spectra of the same substances. Differences arising between reflectance and transmission spectra are attributable, not to the mode of spectroscopy, but to compositional differences between samples. Furthermore, we show that our reflectance FTIRM spectra are consistent with the IR spectra of substances (*e.g.*, collagen and keratin) obtained from an independent reference library. In other words, the reflectance FTIRM reference spectra that we develop in this study are of excellent quality and provide key chemical information about the molecules present in these residues. We provide extensive documentation on the structure and chemical composition of eight characteristic animal residue types, and we

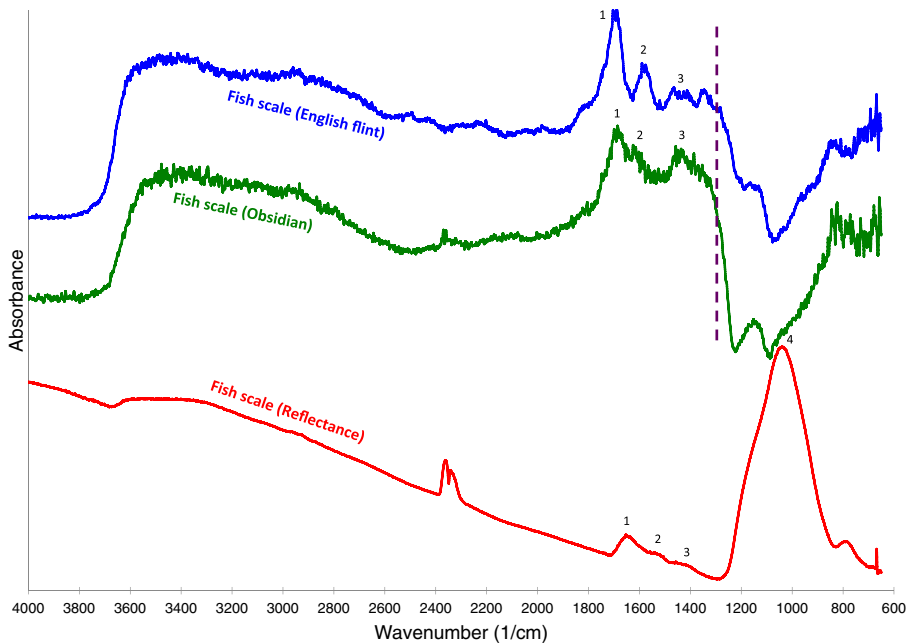


Fig. 16 The FTIR spectra for fish scale on English flint and obsidian compared with the fish scale reflectance standard. The residues on obsidian and flint evidence peak shifts (for peaks 1–3) to higher wavenumbers, relative to the standard (*red line*). The strongest vibrations for hydroxyapatite occur at $\sim 1040\text{ cm}^{-1}$, which falls in the middle of the stones' reststrahlen band and, consequently, appears as a derivative band on the fish scale on stone residues. Peak assignments are in Table 7. All spectra are graphed in calculated absorbance mode ($\log(1/R)$). Note that spectra are plotted on the same scale, but have been vertically offset.

give spectral peak assignments for all of our illustrated spectra in Tables 1, 2, 3, 4, 5, 6, 7, and 8.

We also show that the spectra for animal-tissue residues on stone substrates can be distorted—sometimes severely. The reflectance spectra for skin, meat, blood, and fat residues on stone substrates exhibit derivative peaks in the region of $4000\text{--}1300\text{ cm}^{-1}$. These are due to the fact that the signal which reaches the detector is primarily composed of light specularly reflected from the surface of the residues. Application of the Kramers-Kronig correction makes them comparable with absorbance spectra (in this portion of the spectrum), although distortions remain. Why is this a problem when the residues are located on stone, and not when they are on the mirrored slides? We believe that on the mirrored slides, part of the incident light is specularly reflected from the surface of the residue, while part of it passes *through* the residue. If the residue is thin, the light that has passed through it is reflected from the mirror substrate, and passes through the residue a second time, ultimately reaching the detector. This signal is much stronger than the light that specularly reflected from the residue's surface. Therefore, a typical “absorbance” spectrum is produced. On the other hand, when the residue is located on stone, any light passing through the residue is *not* reflected from the stone (except for the narrow band between $1300\text{ and }1000\text{ cm}^{-1}$ described above); therefore, the entire signal reaching the detector between $4000\text{ and }1300\text{ cm}^{-1}$ is composed of light specularly reflected from the residue surface. The resulting

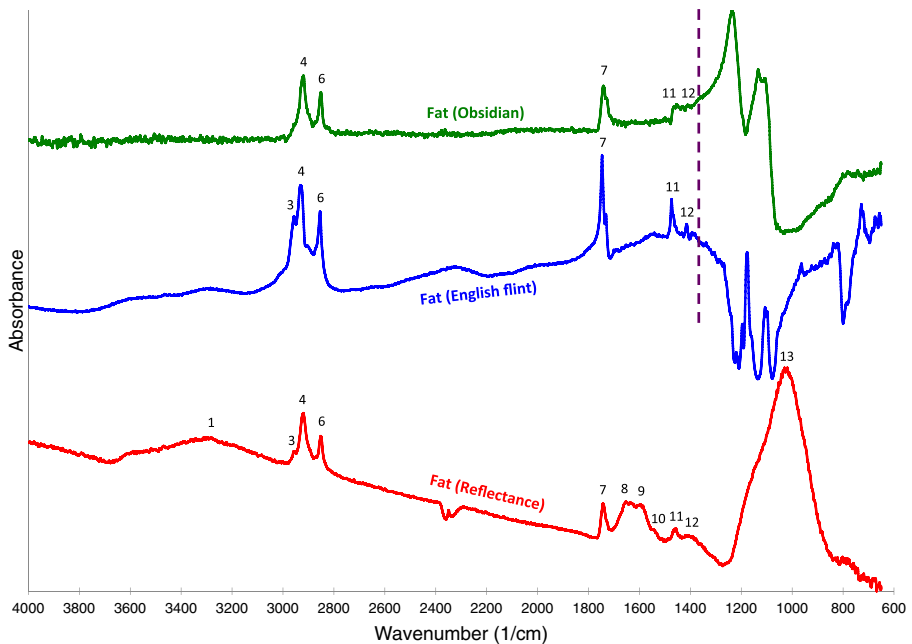


Fig. 17 FTIRM spectra of fat residue on obsidian (Kramers-Kronig transformed) and English flint (not transformed) compared with the fat reflectance standard. Both residue on stone spectra evidence peaks consistent with a high proportion of hydrocarbons (peaks 3–6, 7, 11, and 12; peak assignments are in Table 8). They lack the protein peaks (peaks 8–10) seen in the standard (red line). This compositional difference is attributed to sample preparation differences. Below 1300 cm^{-1} (to the right of the dashed line), the spectra of residues on stone exhibit severe derivative bands. The reflectance standard (red line) and the fat residue on English flint (blue line) are graphed in calculated absorbance mode ($\log(1/R)$). Note that spectra are plotted on the same scale, but have been vertically offset.

spectrum, as we have seen, needs to be corrected. The spectra for feather barbules and calamus, hair, bone, and fish scales on stone do not require a correction. We think this is because these materials exhibit diffuse, rather than specular reflection, which produces absorbance-like spectra.

A complicating factor is that in both cases (*i.e.*, residues exhibiting specular or diffuse reflection), spectra are distorted by the stones' reststrahlen band which occurs between ~ 1300 and 1000 cm^{-1} . This happens regardless of stone type (flint, dacite, chert, or obsidian) because they are all principally composed of SiO_2 and exhibit a major absorbance peak in the range of ~ 1067 – 1084 cm^{-1} (see Fig. 8 in Monnier *et al.* 2017).

Prinsloo *et al.* (2014) argue for using spectra “as is” rather than applying the Kramers-Kronig correction. We counter that this correction is useful because it yields spectra that are comparable with the reflectance standards. In fact, we are able to identify all major peaks between 4000 and 1300 cm^{-1} on all of the residues included in this analysis, though we admit that they are distorted—sometimes severely—relative to the reflectance standards. Below 1300 cm^{-1} , however, many of the spectra we obtained are *not* interpretable due to distortions resulting from the large reststrahlen band of siliceous stone, which cannot be corrected by any algorithm. In some instances, unfortunately, the molecules have their characteristic peaks in this region. Our fat standard, for instance, has a very strong peak at

1029 cm^{-1} attributed to C-O and C-C stretching (Table 8, Fig. 9). This peak is hidden by the flint and obsidian's reststrahlen bands below 1300 cm^{-1} . This is also a problem for animal tissues containing hydroxyapatite, such as bone and fish scale, because the main absorbance peak for this mineral occurs at $\sim 1040 \text{ cm}^{-1}$ (see Tables 6 and 7, and Figs. 7 and 8). Because this is near the location of strongest absorbance for siliceous stone as well, the result is a saturated detector.

In comparing the results from this study to the results from our study of plant residues (Monnier *et al.* 2017), some interesting points emerge. First, none of the plant residue reflectance spectra on stone substrates produced derivative bands. We assume that this is because they exhibit diffuse reflection (like the feathers, hair, bone, and fish scales in this study) rather than specular reflection. Therefore, these spectra do not require a Kramers-Kronig correction and are very similar to the reflectance standards. Second, the spectra produced for plant residues on stone substrates are much less affected by the stone. We did document occasional distortions (see for example Fig. 11 in *ibid.*), but these are usually restricted to the portion of the spectrum below 900 cm^{-1} . We suggest that the diminished effect of the stone on these spectra is due to the fact that the macerated plant tissues were denser and prevented the incident beam from reaching the stone. On the other hand, the macerated animal-tissue residues permitted a strong enough signal to be reflected from the stone that it produced reststrahlen bands in most of the resulting spectra that obliterate the region below 1300 cm^{-1} .

Archeological Implications

The implications of these results for archeological applications are that the nature of the residues (including their thickness and surface texture, as noted by Prinsloo *et al.* 2014) will affect the type of reflectance that will occur, as well as the likelihood that the signal from the stone will be present. This will vary on a case-by-case basis because residues from plant and animal tissues that have been crushed and macerated during use, then subjected to diagenesis, presumably occur in a nearly infinite array of particle sizes and shapes. In this study and our previous one (Monnier *et al.* 2017), we standardized residue preparation across all categories, aiming to produce thin slurries of finely ground particles for the best IR results. It goes without saying that residues on artifacts will not be as homogenous nor nearly as fine. Furthermore, residues are likely to have been dramatically altered by chemical diagenesis, which may affect their optical properties as well.

Therefore, obtaining high-quality reflectance FTIRM spectra on archeological residues will be challenging. This challenge can be mitigated by pushing current instruments to their limits (including reducing aperture sizes to eliminate the stone background and increasing counts to improve the signal-to-noise ratio); developing new instruments with improved capabilities (higher magnification and resolution); and, lastly, removing residues from artifacts when feasible. Taking into account these factors, we are confident that it will be possible to obtain high-quality spectra from ancient residues on stone artifacts. The collection of reference spectra we have developed will help in their analysis.

Finally, because FTIRM is sensitive to intra-sample compositional differences, as we saw for blood (Fig. 4), hair (Fig. 6), and meat (Fig. 3), this means that it has the potential to produce very detailed molecular information. It also means that ancient residues are expected to show compositional differences, relative to our standards, consistent with diagenetic processes such as oxidation and hydrolysis. However, the quality of the

molecular information contained in the spectra (*i.e.*, peak shapes and locations) is commensurate with sample quality and preparation. The degree to which the results produced by *in situ* reflectance FTIRM enable us to distinguish between different types of protein (*e.g.*, keratin versus collagen) will depend upon the size and quality of the residue (including type and degree of degradation) and the quality of the spectra, both of which will be affected by the factors described above. Finally, this sensitivity also means that relatively small quantities of contaminants are needed to alter results, requiring the development of protocols to minimize contamination.

Conclusions

The most secure analyses of organic residues on stone tools involve a convergence of multiple methods, both microscopic and analytical. Reflectance FTIR microspectroscopy has enormous potential in this regard because it produces chemical information non-destructively. Our contribution to the development of this method has been to produce a set of reflectance FTIRM spectra of the animal-tissue residue types most commonly reported in the literature; to document the chemical composition of these residue types and their characteristic vibrations; and to make these reference spectra freely available on our website. Additionally, we systematically document the effects of stone substrates on resulting spectra, discussing the challenges posed by different types of reflection and distortions caused by the infrared signal from siliceous stone.

Future work will be necessary to explore the variability within these different residue types, to document chemical changes arising from decomposition, and to define the limitations of this methodology. Above all, it is important to remember that (1) no single residue analysis methodology is likely to be sufficient—multiple, complementary methods are preferable, especially during this developmental phase; and (2) each archeological site has a unique set of circumstances (raw material types, preservational history, contamination, and so forth) that will require adjustment of residue analysis methodologies to provide the most accurate identifications. This means that lithic residue analysis will never be a speedy endeavor; however, continued development of residue analysis methodologies will undoubtedly yield more secure results and provide new insights into hominin tool-using behaviors.

Acknowledgements This work was funded by NSF grant # BCS-1420702. It was carried out at the University of Minnesota in the Evolutionary Anthropology Laboratories and in the Characterization Facility, which receives partial support from the NSF through the MRSEC program. Many thanks to Matt Edling, Greg Haugstad, Keith Manthie, Colin McFadden, Marjorie Schalles, Nora Last, Kara Kersteter, and Gil Tostevin. Thanks also to the three anonymous reviewers whose comments and suggestions helped improve the final manuscript.

References

- Acerbo, A. S., Carr, G. L., Judex, S., & Miller, L. M. (2012). Imaging the material properties of bone specimens using reflection-based infrared microspectroscopy. *Analytical Chemistry*, *84*, 3607–3613.
- Baddiel, C. B. (1968). Structure and reactions of human hair keratin: an analysis by infrared spectroscopy. *Journal of Molecular Biology*, *38*, 181–199.
- Barth, A. (2007). Infrared spectroscopy of proteins. *Biochimica et Biophysica Acta*, *1767*, 1073–1101.

- Calabrò, E., & Magazù, S. (2014). Non-thermal effects of microwave oven heating on ground beef meat studied in the mid-infrared region by Fourier transform infrared spectroscopy. *Spectroscopy Letters*, *47*, 649–656.
- Cesaro, S. N., & Lemorini, C. (2012). The function of prehistoric lithic tools: a combined study of use-wear analysis and FTIR microspectroscopy. *Spectrochimica Acta Part A-Molecular and Biomolecular Spectroscopy*, *86*, 299–304.
- Chapman, R. E. (1986). Chapter 17: hair, wool, quill, nail, claw, hoof, and horn, in part VI: the skin of mammals. In J. Bereiter-Hahn, A. G. Matoltsy, & K. Sylvia Richards (Eds.), *Biology of the integument, part 2: vertebrates* (pp. 293–317). Berlin: Springer-Verlag.
- Croft, S., Monnier, G. F., Radini, A., Little, A., & Milner, N. (2016). Lithic residue survival and characterisation at Star Carr: a burial experiment. *Internet Archaeology*, 1–88.
- Crowther, A. Haslam, M., Oakden, N., Walde, D., & Mercader, J. (2014). Documenting contamination in ancient starch laboratories. *Journal of Archaeological Science*, *49*, 90–104.
- Deleris, G., & Petibois, C. (2003). Applications of FT-IR spectrometry to plasma contents analysis and monitoring. *Vibrational Spectroscopy*, *32*, 129–136.
- Duarte, R., Simoes, M., & Sgarbieri, V. (1999). Bovine blood components: fractionation, composition, and nutritive value. *Journal of Agricultural and Food Chemistry*, *47*, 231–236.
- Feughelman, M. (1997). *Mechanical properties and structure of alpha-keratin fibres: wool, human hair, and related fibres*. Sydney: University of New South Wales Press.
- Finlayson, C., Brown, K., Blasco, R., Rosell, J., Jose Negro, J., Bortolotti, G. R., et al. (2012). Birds of a feather: Neanderthal exploitation of raptors and corvids. *PLoS One*, *7*, e45927.
- Fowler, B. O. (1974). Infrared studies of apatites. I. Vibrational assignments for calcium, strontium, and barium hydroxyapatites utilizing isotopic substitution. *Inorganic Chemistry*, *13*(1), 194–207.
- Fraser, R. D. B., & Parry, D. A. D. (2008). Molecular packing in the feather keratin filament. *Journal of Structural Biology*, *162*, 1–13.
- Fronticelli, C., Sanna, M., Perez-Alvarado, G., Karavitis, M., Lu, A., & Brinigar, W. (1995). Allosteric modulation by tertiary structure in mammalian hemoglobins—introduction of the functional characteristics of bovine hemoglobin into human hemoglobin by five amino acid substitutions. *Journal of Biological Chemistry*, *270*, 30588–30592.
- Greenwold, M. J., & Sawyer, R. H. (2011). Linking the molecular evolution of avian beta (beta) keratins to the evolution of feathers. *Journal of Experimental Zoology Part B-Molecular and Developmental Evolution*, *316B*, 609–616.
- Gregg, K., & Rogers, G. E. (1986). Chapter 33: feather keratin: composition, structure and biogenesis, in part XIII: skin proteins. In J. Bereiter-Hahn, A. G. Matoltsy, & K. Sylvia Richards (Eds.), *Biology of the integument, part 2: vertebrates* (pp. 666–694). Berlin: Springer-Verlag.
- Hardy, B. L. (2004). Neanderthal behaviour and stone tool function at the middle Palaeolithic site of La Quina, France. *Antiquity*, *78*, 547–565.
- Hardy, B. L., & Moncel, M. (2011). Neanderthal use of fish, mammals, birds, starchy plants and wood 125–250,000 years ago. *PLoS One*, *6*, e23768.
- Hardy, B. L., Kay, M., Marks, A. E., & Monigal, K. (2001). Stone tool function at the Paleolithic sites of Starosele and Buran Kaya III, Crimea: behavioral implications. *Proceedings of the National Academy of Sciences of the United States of America*, *98*, 10972–10977.
- Hardy, B. L., Bolus, M., & Conard, N. J. (2008). Hammer or crescent wrench? Stone-tool form and function in the Aurignacian of southwest Germany. *Journal of Human Evolution*, *54*, 648–662.
- Hardy, B.L., Moncel, M., Daujeard, C., Fernandes, P., Béarez, P., Desclaux, E., et al., 2013. Impossible Neanderthals? Making string, throwing projectiles and catching small game during marine isotope stage 4 (Abri du Maras, France). *Quaternary Science Reviews*, *82*, 23–40.
- Hortolà, P. (2016). Human bloodstains on bone artefacts: an SEM intra- and inter-sample comparative study using ratite bird tibiotarsus. *Micron*, *90*, 108–113.
- Ikoma, T., Kobayashi, H., Tanaka, J., Walsh, D., & Mann, S. (2003). Microstructure, mechanical, and biomimetic properties of fish scales from *Pagrus major*. *Journal of Structural Biology*, *142*, 327–333.
- Jung, C. (2000). Insight into protein structure and protein-ligand recognition by Fourier transform infrared spectroscopy. *Journal of Molecular Recognition*, *13*, 325–351.
- Kolczynska-Szafraniec, U., & Bilińska, B. (1993). Infrared studies of natural pheomelanins. *Current Topics in Biophysics*, *16*(2), 77–80.
- Kreplak, L., Doucet, J., Dumas, P., & Briki, F. (2004). New aspects of the alpha-helix to beta-sheet transition in stretched hard alpha-keratin fibers. *Biophysical Journal*, *87*, 640–647.
- Langejans, G. (2010). Remains of the day—preservation of organic micro-residues on stone tools. *Journal of Archaeological Science*, *37*, 971–985.

- Langejans, G. (2011). Discerning use-related micro-residues on tools. Testing the multi-stranded approach for archaeological studies. *Journal of Archaeological Science*, *38*, 985–1000.
- Lieber, R. L. (2002). Skeletal muscle structure, function, and plasticity. In *The physiological basis of rehabilitation* (2nd ed.). Philadelphia: Lippincott, Williams, & Wilkins.
- Lombard, M. (2005). Evidence of hunting and hafting during the Middle Stone age at Sibidu Cave, KwaZulu-Natal, South Africa: a multianalytical approach. *Journal of Human Evolution*, *48*, 279–300.
- Lombard, M. (2008). Finding resolution for the Howiesons Poort through the microscope: micro-residue analysis of segments from Sibudu Cave, South Africa. *Journal of Archaeological Science*, *35*, 26–41.
- Lombard, M. (2011). Quartz-tipped arrows older than 60 ka: further use-trace evidence from Sibudu, KwaZulu-Natal, South Africa RID A-2444-2012. *Journal of Archaeological Science*, *38*, 1918–1930.
- Lombard, M. (2014). In situ presumptive test for blood residues applied to 62,000-year-old stone tools. *South African Archaeological Bulletin*, *69*, 80–86.
- Loy, T., & Dixon, E. (1998). Blood residues on fluted points from eastern Beringia. *American Antiquity*, *63*, 21–46.
- Loy, T. H., & Hardy, B. L. (1992). Blood residue analysis of 90,000-year-old stone tools from Tabun Cave, Israel. *Antiquity*, *66*, 24–35.
- Matoltsy, A. G. (1986a). Chapter 14 in biology of the integument 2: vertebrates. In J. Bereiter-Hahn, A. G. Matoltsy, & K. Sylvia Richards (Eds.), *Structure and function of the mammalian epidermis* (pp. 255–271). Berlin: Springer-Verlag.
- Matoltsy, A. G. (1986b). Chapter 15 in biology of the integument 2: vertebrates. In J. Bereiter-Hahn, A. G. Matoltsy, & K. Sylvia Richards (Eds.), *Dermis* (pp. 272–277). Berlin: Springer-Verlag.
- Miyazawa, T., Shimanouchi, T., & Mizushima, S. (1958). Normal vibrations of N-methylacetamide. *The Journal of Chemical Physics*, *29*(3), 611–616.
- Monnier, G. F., Ladwig, J. L., & Porter, S. T. (2012). Swept under the rug: the problem of unacknowledged ambiguity in lithic residue identification. *Journal of Archaeological Science*, *39*, 3284–3300.
- Monnier, G. F., Hauck, T. C., Feinberg, J. M., Luo, B., Le Tensorer, J., & al Sakhel, H. (2013). A multi-analytical methodology of lithic residue analysis applied to Paleolithic tools from Hummal, Syria. *Journal of Archaeological Science*, *40*, 3722–3739.
- Monnier, G. F., Frahm, E., Luo, B., & Missal, K. (2017). Developing FTIR microspectroscopy for analysis of plant residues on stone tools. *Journal of Archaeological Science*, *78*, 158–178.
- Morin, E., & Laroulandie, V. (2012). Presumed symbolic use of diurnal raptors by Neanderthals. *PLoS One*, *7*, e32856.
- Pearson, J. F., & Slifkin, M. A. (1972). The infrared spectra of amino acids and dipeptides. *Spectrochimica Acta*, *Vol.*, *28A*, 2408–2417.
- Pederghana, A., Asryan, L., Fernández-Marchena, J. L., & Ollé, A. (2016). Modern contaminants affecting microscopic residue analysis on stone tools: A word of caution. *Micron*, *86*, 1–21.
- Powell, B. C., & Rogers, G. E. (1986). Chapter 34: hair keratin: composition, structure, and biogenesis, in part XIII: skin proteins. In J. Bereiter-Hahn, A. G. Matoltsy, & K. Sylvia Richards (Eds.), *Biology of the integument, part 2: vertebrates* (pp. 695–721). Berlin: Springer-Verlag.
- Prinsloo, L. C., Wadley, L., & Lombard, M. (2014). Infrared reflectance spectroscopy as an analytical technique for the study of residues on stone tools: potential and challenges. *Journal of Archaeological Science*, *41*, 732–739.
- Rahmania, H., Sudjadi, & Rohman, A. (2015). The employment of FTIR spectroscopy in combination with chemometrics for analysis of rat meat in meatball formulation. *Meat Science*, *100*, 301–305.
- Rao, C. N. R., & Venkataraghavan, R. (1963). Contribution to the infrared spectra of five-membered N- and N,S-heterocyclic compounds. *Canadian Journal of Chemistry*, *42*, 43–49.
- Rehman, I., & Bonfield, W. (1997). Characterization of hydroxyapatite and carbonated apatite by photo acoustic FTIR spectroscopy. *Journal of Materials Science-Materials in Medicine*, *8*, 1–4.
- Robertson, G., Attenbrow, V., & Hiscock, P. (2009). Multiple uses for Australian backed artefacts. *Antiquity*, *83*, 296–308.
- Sobolik, K. (1996). Lithic organic residue analysis: an example from the southwestern archaic. *Journal of Field Archaeology*, *23*, 461–469.
- Solodenko, N., Zupancich, A., Cesaro, S. N., Marder, O., Lemorini, C., & Barkai, R. (2015). Fat residue and use-wear found on Acheulian Biface and scraper associated with butchered elephant remains at the site of Revadim, Israel. *PLoS One*, *10*(3): e0118572. doi:10.1371/journal.pone.0118572.
- Stephenson, B. (2015). A modified Picro-Sirius Red (PSR) staining procedure with polarization microscopy for identifying collagen in archaeological residues. *Journal of Archaeological Science*, *61*, 235–243.
- Stettenheim, P. (2000). The integumentary morphology of modern birds—an overview. *American Zoologist*, *40*, 461–477.

- Stiner, M., Weiner, S., Bar-Yosef, O., & Kuhn, S. L. (1995). Differential burning, fragmentation, and preservation of archaeological bone. *Journal of Archaeological Science*, *22*, 223–237.
- Stiner, M., Kuhn, S., Surovell, T., Goldberg, P., Meignen, L., Weiner, S., et al. (2001). Bone preservation in Hayonim Cave (Israel): a macroscopic and mineralogical study. *Journal of Archaeological Science*, *28*, 643–659.
- Suzuki, S., Ohshima, T., Tamiya, N., Fukushima, K., Shimanouchi, T., & Mizushima, S. (1959). Infrared spectra of deuterated α -amino acids $\text{NH}_3^+\text{CDRCOO}^-$. Assignment of the absorption bands of α -alanine. *Spectrochimica Acta*, *11*, 969–976.
- Uitto, J. (1986). Chapter 40 in biology of the integument 2: vertebrates. In J. Bereiter-Hahn, A. G. Matoltsy, & K. Sylvia Richards (Eds.), *Interstitial collagens* (pp. 800–809). Berlin: Springer-Verlag.
- Vlachos, N., Skopelitis, Y., Psaroudaki, M., Konstantinidou, V., Chatzilazarou, A., & Tegou, E. (2006). Applications of Fourier transform-infrared spectroscopy to edible oils. *Analytica Chimica Acta*, *573*, 459–465.
- Warriss, P. D. (2010). Meat science, 2nd edition. In *An introductory text*. Oxfordshire, U.K.: CABI.
- Weiner, S. (2010). *Microarchaeology: beyond the visible archaeological record*. Cambridge, U.K.: Cambridge University Press.
- Williamson, B. (2004). Middle stone age tool function from residue analysis at Sibudu Cave. *South African Journal of Science*, *100*, 174–178.
- Zylberberg, L., Bereiter-Hahn, J., & Sire, J.-Y. (1988). Cytoskeletal organization and collagen orientation in the fish scales. *Cell and Tissue Research*, *253*, 597–607.